Grímsvötn ash layers, a 3D modeling GPR investigation of the englacial debris within the Vatnajökull ice cap

Daniel Dehlin
Ivan Morales

Degree of Bachelor of Science
with a major in Earth Sciences
15 hec

Department of Earth Sciences
University of Gothenburg
2020 B-1087

Faculty of Science

UNIVERSITY OF GOTHENBURG

UNIVERSITY OF GOTHENBURG
Department of Earth Sciences
Geovetarcentrum/Earth Science Centre

Grímsvötn ash layers, a 3D modeling GPR investigation of the englacial debris within the Vatnajökull ice cap

Daniel Dehlin
Ivan Morales

ISSN 1400-3821

B1087
Bachelor of Science thesis
Göteborg 2020

Mailing address
Geovetarcentrum
S 405 30 Göteborg

Address
Geovetarcentrum
Guldhedsgatan 5A

Telephone
031-786 19 56

Geovetarcentrum
Göteborg University
S-405 30 Göteborg
SWEDEN

Abstract

In this report, three-dimensional (3D) modeling is used to facilitate Ground Penetrating Radar (GPR) imagery of the Vatnajökull ice cap, finding and mapping the englacial layers of tephra recorded in the stratigraphy above Grímsvötn, Iceland's most active subglacial volcano. GPR measurements together with 3D modeling, and 2D fracture mapping has proven to be an excellent combination for these types of investigations, showing significant results in visualizing how the volcanic layers and fractures are distributed throughout the recrystallized snow and ice held within the caldera.

Through the course of the project, a more complete modeling methodology has been developed, based on earlier work of 3D modeling and research data provided from Iceland, enabling a detailed visual investigation of the dynamics between Grímsvötn and Vatnajökull.

GPR measurements show that the ash remnants of the 2004 and 2011 eruptions can be observed in most of the stratigraphy at the site of Grímsvötn, and hyperbola mapping reveal a connection between the surface topography and subsurface fractures. From modeling, an estimation of sequence thicknesses and snow/ice accumulation has been made, and general inspection reveals lower ice and snow thickness between the years 2004-2011 compared to years 2011-2019 due to the effects of compaction. On closer inspection, the two ash layers each have a ‘unique topography’ and are found buried at alternating depths throughout the caldera glacier. General mass accumulation appears greatest at the caldera rims and lower at the caldera center, but modeling reveals that there is a differing pattern of volume accumulation and/or compaction seen at the south caldera wall, where the 2011 ash layer is buried beneath 17 to 20 meters of combined ice and recrystallized snow, while the 2004 layer has a slim burial of 5-6 meters from the layer above. This difference is explained by compression gradients caused by Vatnajökull’s southward flowing movements into the caldera, as well as added snow and ice cover provided at the southern caldera wall (where avalanches are more prone and midday sun exposure is low). Thermal heat flux at the caldera edges post eruption may also have quickened the ice melt above the 2004 ash layer to the south, an idea supported by the discovery of fractures and associated surface depressions along the south wall, likely formed as a response to hydrothermal activity from the volcano below.

Based on the results provided in this report it is concluded that the differences in ice and snow thickness over the sections within Vatnajökull are largely a result of the dynamic interaction between the Vatnajökull ice cap and the active volcano below it. Furthermore, interaction between the glacier and the caldera meltwater is believed generate the same or more melting than the climatic conditions on the surface.

Acknowledgements

Here we would like to acknowledge our advisor Erik Sturkell who managed to provide an interesting and thought provoking project at such short notice when our previous project was put on hold, inspiring us do this work of which we are immensely proud. We would also like to thank Finnur Pálsson, Eyjólfur Magnússon, Andrea Håkansson, Jon Kjartansson and all their helping colleagues for their hard work, providing us with valuable data and information, without which none of this would have been possible. To Mark Johnson and colleagues for their good advice and without doubt to our families who were always supporting us and giving us love.

Table of Contents

1. Introduction

Ash layers make for excellent chronostratigraphic markers, as they represent a same-age surface that can be used as reference when making scientific observations of change within glacier stratigraphy.

Ground Penetrating Radar (GPR) is a useful tool when investigating the subsurface, as it facilitates a looking glass into the interior of a multitude of different types of terrain. In this article, a three-dimensional (3D) modeling technique has been explored in hopes of estimating more accurately what can be seen in the interior of the Vatnajökull ice above Grímsvötn. With the combined advantages of GPR imagery and 3D modeling this thesis attempts to demonstrate the possibilities of investigating pyroclastic debris buried in ice, while also trying to provide new information about this particular glacier system. At the present time, as technologies advance, 3D modeling is growing more and more common within different areas of geological investigation.

In this report, the word “ice” will be used as a generalization of the whole thickness of the Vatnajökull glacier. In some places it will be used referring to the compacted and recrystallized snow not yet turned into glacial ice, but also referring to the the glacial ice itself. Because Grímsvötn is a complex warm based glacier, it is difficult to know at what depth the “ice” mass within the caldera turns into glacial ice.

1.1 Geological Background

Grímsvötn is a basaltic subglacial volcano situated in the south-western parts of the Vatnajökull ice cap, and has a summit at 1719 m.a.s.l., north of an area called Háabunga (Global Volcanism Program, 2011) (see *Figure. 1.1*). The caldera contains a meltwater lake sustained by geothermal heat and subglacial melting produced under the geothermal activity of the volcano (Björnsson, 2003; Institute of Earth Sciences, n.d.).

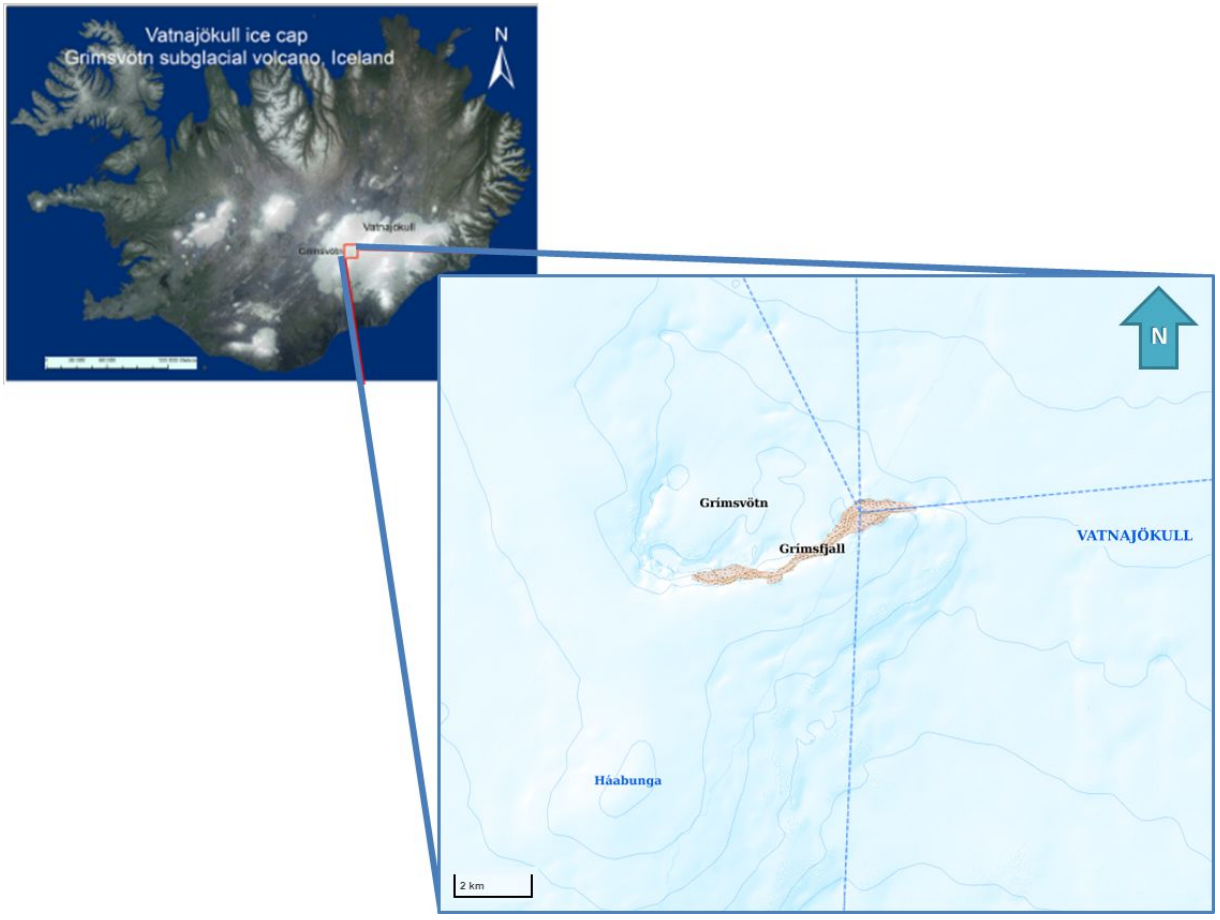

Figure 1.1: *Overview of the study area showing Grímsvötn in relation to Háabunga at Vatnajökull, Iceland. Based on data from National Land Survey of Iceland (2020).*

The caldera lake at Grímsvötn is part subglacial and part subareal (Gudmundsson, Högnadóttir, Pálsson & Reynolds, 2018). The subareal part is positioned in the south west corner of the crater, where the underlying bedrock topography is especially elevated above the caldera floor (Gudmundsson, 1989). The lake is intermittently drained during sudden glacial outburst floods (jökulhlaups) that have been known to disrupt transport lanes between the capital and south-east of Iceland (Benn & Evans, 2013). Sudden drops in the water level have previously served as precursor indicators before volcanic eruptions (Institute of Earth Sciences, n.d.). Work summarized by Gudmundsson et. al. (2018) show that the lake-level changes within the Grímsvötn caldera vary greatly with time and that the water mass creates a glacial uplift of the floating ice. This glacial uplift is turned backwards every 1-10 years as the lake water subglacial drains (Benn & Evans, 2013).

In June, 2019, the lake level was positioned at 1371.1 m.a.s.l. as reported by Magnússon (personal communication 21st April 2020), a value taken from GPS measurement on the glacier free part of the lake.

1.1.1 The 2004 and 2011 Eruptions

In November 2004, a six-day long eruption was triggered when the release of overburden pressure was caused by a jökulhlaup draining of the subglacial lake (Institute of Earth Sciences, n.d.). According to Oddsson, (2007) the eruption started on the first of November and was confirmed when a volcanic plume of ash and steam broke through the glacier-ice and rose 7-10 kilometers above the Grímsvötn caldera. Other sources (Institute of Earth Sciences, n.d.) report the maximum altitude of the plume as to reaching 13-14 km into the stratosphere that was visible across northern Scandinavia. The eruption left behind an ice cauldron and a crater lake surrounded by tephra, as shown in *Figure 1.2*. (Oddsson, 2007), and reports of ash falls were given reaching a minimum distance of 150 km from the crater (Institute of Earth Sciences, n.d.).

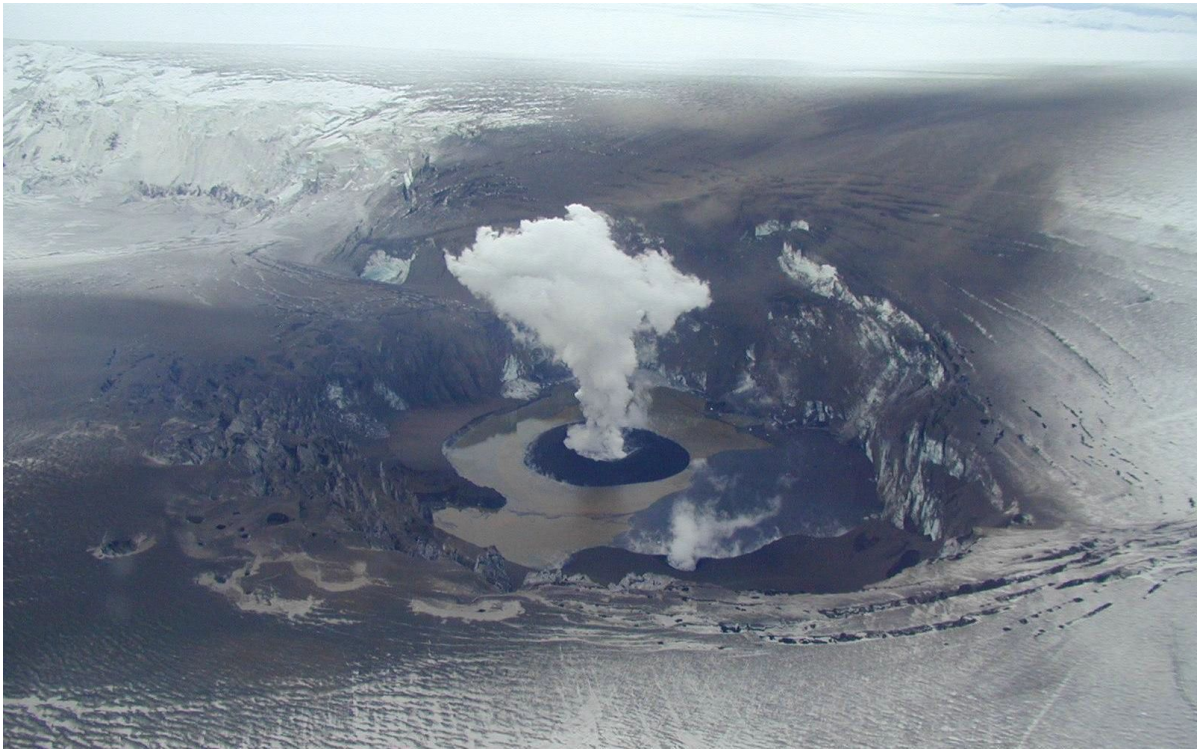

Figure 1.2: *Photograph showing the ice cauldron formed during the 2004 eruption, the broken icefield around the crater and the tephra pile formed during the last eruptive phase. Here the south-west winds lead the plume in direction toward the north-east part of Vatnajökull. Photo by Snæbjörn Guðbjörnsson. Oddsson B. (2007).*

On May 21, 2011, the most recent volcanic eruption occured. Within the span of a few hours the plume of volcanic material had risen to an altitude of twenty kilometers above the caldera (NASA, 2011). The following days saw ash falls descending over large parts of the country with low-level winds dragging a trail of volcanic sediment in a north-easterly direction (see *Figure 1.3*) (Petersen et. al., 2012), as was seen in 2004 (Institute of Earth Sciences, n.d.). According to Håkansson (2019) and Sturkell

(personal communication, May 2020) thick ash debris was also deposited south-west of the caldera in Háabunga.

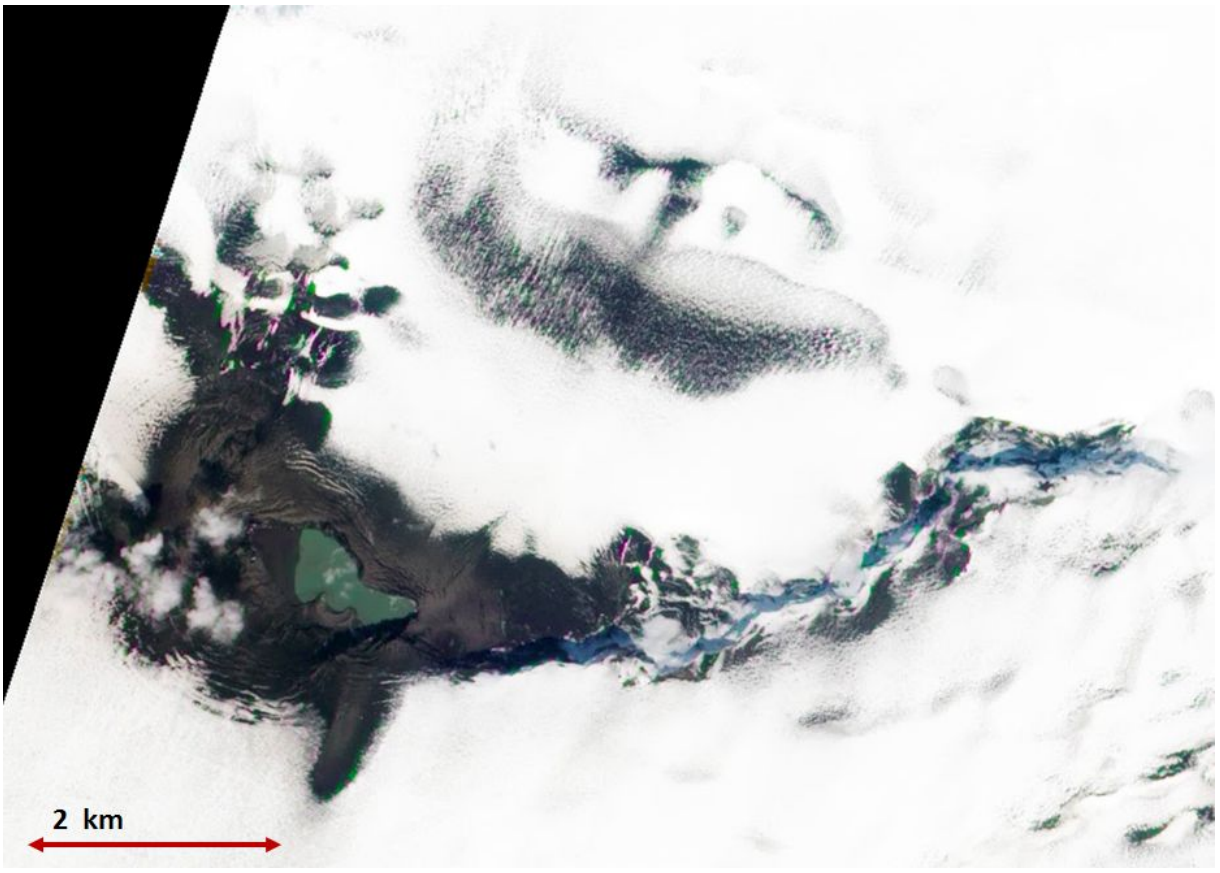

Figure 1.3: *Grímsvötn caldera meltwater lake in June 11, 2011 roughly one month post eruption. Here the ash has already begun to bury beneath the snow. Image has been borrowed from NASA Earth Observatory (2011) and added with a scale based on Figure 1.1.*

Glacier systems are morphologically complex, as budgets of mass and energy are always changing (Benn & Evans, 2013). Nearly a decade after the most recent eruption, most of the volcanic features evident from the event have been fully or partly buried by repeated winter snows, and much of the caldera lake has yet again become dammed beneath the ice cap (NASA, 2011), thereby temporarily keeping future volcanic eruptions in check. But, Grímsvötn -- being the most active volcano on Iceland -- ensures a continuous supply of geothermal heat exchange between the subglacial melt lake and the cold underbelly of the ice (NASA, 2004; NASA, 2011; Gudmundsson et. al., 2018).

1.2 Ground Penetrating Radar (GPR)

GPR is an electromagnetic measurement tool with the aim to see beneath the surface, applied in various different disciplines such as groundwater contamination, sedimentology, glaciology, geotechnical engineering and archeology (Jol, 2008). The GPR method consists of a transmitting antenna sending out electromagnetic signals through the earth and a receiving antenna that receives the reflected signals and

sends them to be stored and displayed at the monitor. Sometimes, as in the case of a Rough Terrain Antenna (RTA), the receiver and transmitter can part of the same device (Guideline Geo, 2011).

Wavelength and frequency are intimately related, and the depth and resolution of the data are therefore directly governed by the choice of antenna. There are two reasons: (1) the signal loses more energy before bounce back the further down into the subsurface it reaches, and (2) the GPR is only able to clearly distinguish between features of sizes larger than half the signal wavelength. High frequency antennas therefore reveal high resolution data at the cost of low penetration depth, while the opposite is true for low frequency antennas where resolution is low, but penetration depth is high. (Khan & Mussett, 2000)

The efficiency of GPR subsurface layer detection depends on the electromagnetic behaviour of the earth materials encountered by the signal, and some materials conduct the transmitted waves better than others, allowing different signal velocities (Jol, 2008; Khan & Musset, 2000). Ice and snow are known to be good at transmitting radar signals (Sturkell, personal communication, 2020)

When a travelling electromagnetic signal encounters a sudden change of material properties (permittivity and/or electrical conductivity) between two layers, part of the signal will be reflected, refracted or scattered toward the surface where it can be received by a GPR receiver antenna (Håkansson, 2019). If there is a high enough contrast between material properties eg. comparing ice, firn or snow to ash, then the reflected signal may be distinguishable and identified as a ‘reflector’.

1.3 Previous GPR investigations in Háabunga

In this thesis, GPR was applied over the Vatnajökull glacier in Iceland, with the aim of seeing through the ice. Such application of the GPR has proven fruitful in the area of Grímsvötn in the past, as reported by Håkansson (2019). In her master’s thesis study, Håkansson, by utilizing the geophysical method of GPR, was able to detect ash layer deposits from the volcanic eruption of Grímsvötn in 2011. In her work she demonstrates that the 2011 Ash layer in Háabunga varies in depth. Using a Common Mid-Point (CMP) analysis (an accurate GPR method used to determine the signal velocities through multiple layers in the subsurface) she was able to determine the layer velocities of the ash and ice layers in the area of Háabunga. With this information GPR software was able to provide better data accuracy than if standardized table velocities had been used.

Håkansson (2019) was able to present a three-layer velocity model of the ice and the ash layer just south of the caldera, where the ash accumulation reached thickness up to one meter. In her study, ash-signal reflections from the 2004 volcanic eruption of Grímsvötn were not found.

Håkansson (2019) also showed that GPR can be a useful tool for discerning hollows and fractures within the ice.

1.4 June ice core

In June 2019, Finnur Pálsson and his team on Iceland extracted a 13.1 m long ice core at a drill site positioned on the ice within the caldera (Pálsson, 2019) (*Figure 1.4*). Pálsson's ice core reached down to 1415 m.a.s.l. (absolute elevation value from 2019) and encountered various ice lenses and thin layers of tephra. According to Sturkell (personal communication, May 2020) the core was extracted at a conveniently chosen location close to a measuring site, but digging did not go deep enough to encounter the 2004 layer. Tightly packed and thin layers of tephra encountered in the core are therefore likely wind-driven debris of 2011 ash re-deposited during seasonal melting.

Figure 1.4: *Labeled photograph of the 2019 ice core in June in the Grímsvötn caldera, showing layers of ash. Photograph courtesy of Pálsson (2020).*

1.5 Aim

This thesis aims to investigate the chronostratigraphic markers of the Vatnajökull glacier held within the Grímsvötn caldera, by presenting and evaluating a three-dimensional Ground Penetrating Radar (GPR) model of the ash layers formed after the two most recent volcanic eruptions.

The article will attempt to answer the following questions:

- *How are the ash layers from the most recent volcanic eruptions distributed within the glacier in the Grímsvötn caldera?*

- *How has the snow and ice accumulated and compacted between and after the volcanic eruptions?*

- *Are there any distinguishable crevasses in the glacier represented by indicative hyperbolas in the GPR data? If so, what is the spatial distribution of these?*

2. Methods

The overarching methodology of this modeling report was to work with the GPR, GPS and elevation data recorded from Vatnajökull and Grímsvötn in Iceland. GPR and GPS data sets used in this thesis were provided courtesy of Professor Erik Sturkell, at the Department of Geosciences in Gothenburg, Sweden, and Finnur Pálsson and Eyjólfur Magnússon from the University of Iceland.

2.1 Measurements and Setup

The measurements within the Grímsvötn caldera were made in June, 2019 providing GPR and GPS data along gridded tracks within the caldera (Sturkell, personal communication, Marsh 2020). east-west profiles were spaced 50-150 meters between each other, and the north-south profiles had a spacing of approximately 100 to 500 meters (*Figure 2.1*).

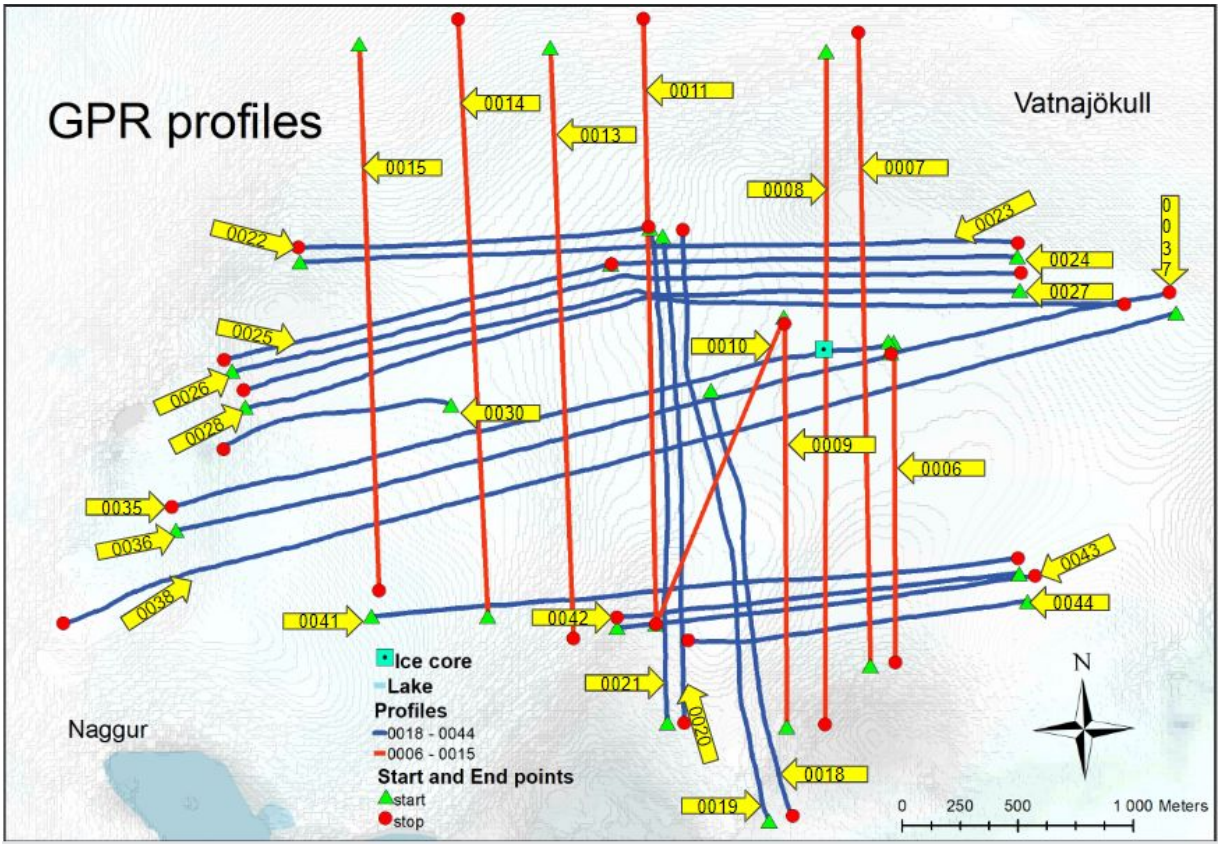

Figure 2.1: *GPR track chart showing profile relationships and placement in relation to the June ice core and the lake at Naggur. Profiles in the red color are those without navigation data and in the blue color are those with navigation data. Note that "Naggur" is the name of the topographic bedrock elevation below the ice and not the lake. DEM background based on data from National Land Survey of Iceland.*

The GPR data was extracted using a 50 MHz shielded Rough Terrain Antenna (RTA), a Malå RAMAC/GPR CU II control unit and a standard coupled XV monitor. The antenna was towed behind a sled coupled to a snow scooter and dragged along the profile grid (*Figure. 2.2*) (Sturkell, personal communication, April 2020). The fieldwork resulted in 29 GPR profiles in workable condition.

Figure 2.2: *GPR setup from summer 2019 with RTA antenna (yellow cord) and measuring wheel coupled to a sled behind a snowmobile. Photo courtesy of Professor Erik Sturkell & Jon Kjartansson (2020).*

2.2 Handling GPS coordinates in GIS

The received GPS dataset is a collection of gridded coordinate points containing the measurements within the caldera and was provided as gpx tables using the EPSG 3057 coordinate system. Additionally, a separate Excel document was provided containing beginning and end positions for each of the individual profiles. These coordinates had to be manually adjusted in ArcMap to match the navigational data provided by in the gpx files. After identifying the profiles, removing all unrelated data and matching the profiles along these points, new attribute tables containing longitude and latitude data were exported in the appropriate ASCII-file formatting. The navigation tracks along the profiles could then be cut out of a high-resolution DEM (4x4 m), (assistance provided by Magnússon, 2020) in order to provide the elevational data for the points along each profile. This elevation data, along with positional coordinates would later be used in the software ReflexW to get the GPR corrected for elevation.

Due to loss of high resolution navigational data along several of the 29 profiles, much of the elevation data going primarily in the rough N-S direction could only be extracted out of the DEM along a straight track from start to end (see north-south

facing profiles in *Figure 2.1*), thereby resulting in a loss of precision along these particular lanes. The value of the data from these profiles was nonetheless included in the following processing as their informational value were considered high enough to outweigh their adding to the margin of error.

2.3 GPR data processing

The GPR data was processed in ReflexW, a GPR and seismic processing software. The software was used for correcting for elevation as well as for filtering of the profiles in order to produce better resolution images. The data filtration steps taken are exemplified in *Figure 2.3*.

2.3.1 Filtering

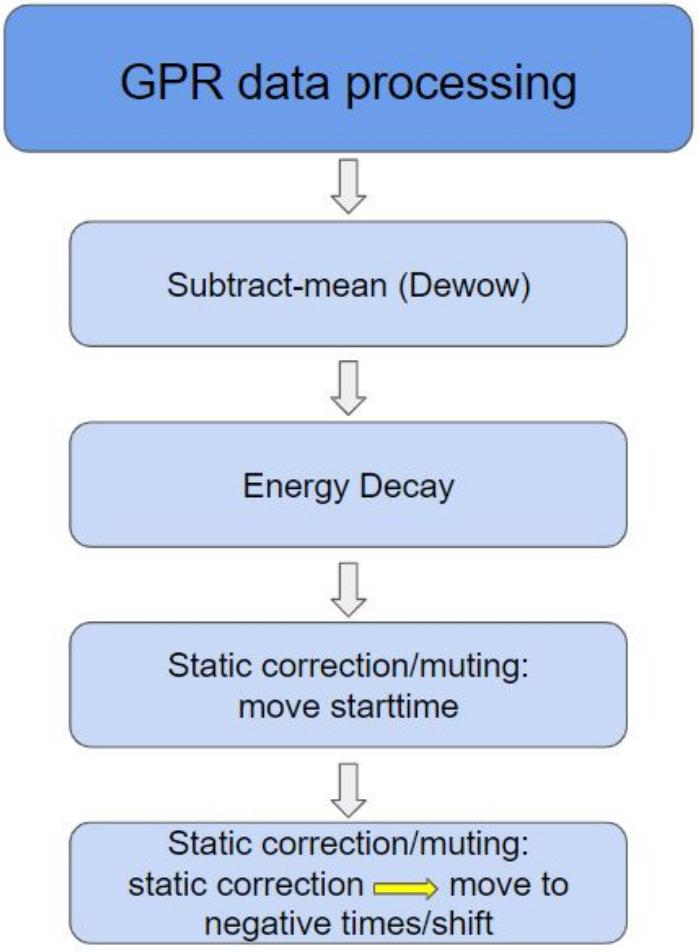

Figure 2.3: *Order of data filtration steps taken in ReflexW. (1) Subtract-mean (Dewow), (2) Energy Decay, (3-4) Move Start Time and Static Correction. Parameters used for Dewow and Energy Decay were 20 and 1 respectively. The subtraction of the air wave and the direct ground wave were done at -80ns with Move Start Time (see Figure 2.4. for illustration).*

Subtract-mean (Dewow) removed the “wow” component (DC-bias) of the GPR signal caused by the proximity of the antennas. This is a low frequency bias of the mean amplitude of the waveform (C.Rowell, 2011). The *Energy Decay* function was used to

compensate for the natural signal loss over time/depth (Sandmeier, 2020), and The "*Move Start Time"* function was used to remove the direct air and ground waves in each profile (*Figure 2.4*).

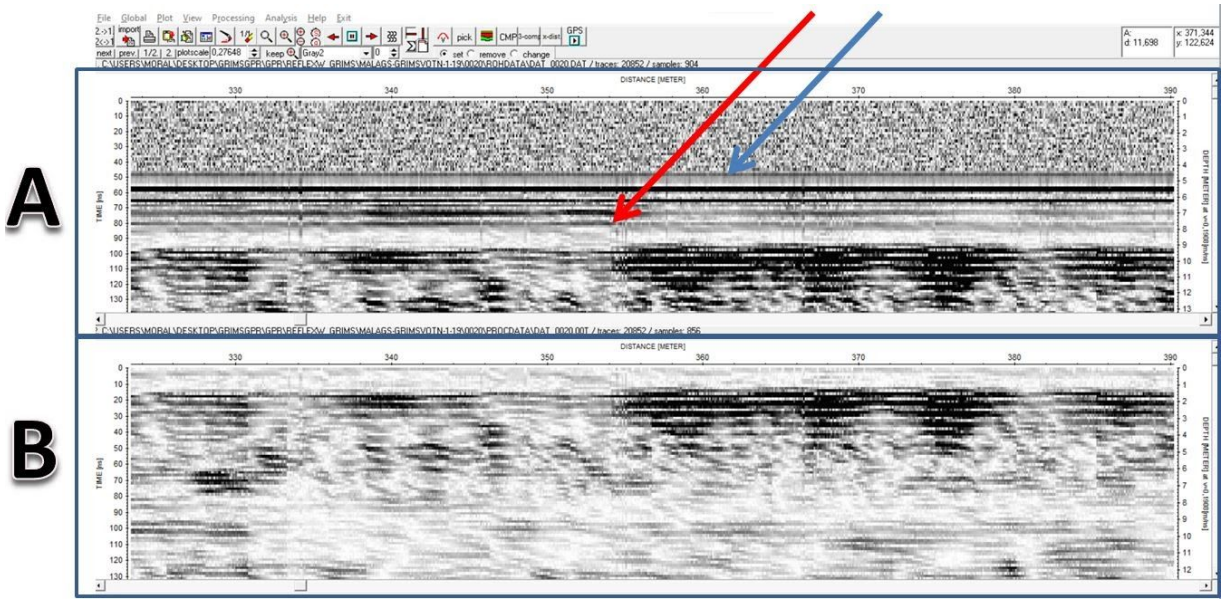

Figure 2.4: *GPR profile example before (A) and after (B) removal of the direct air wave (above the blue arrow) and the direct ground wave (above the red arrow).*

The amplitude scale was adjusted in a case by case value for each profile, enabling enough contrast to observe the layers of interest. The maximum elevation of each profile was used as reference for an absolute depth m.a.s.l. instead of relative values for easy comparison.

2.3.2 Elevation correction

Elevational data was used to correct for the change of topography along each profile. These were first converted using a standard velocity equation (2.1), where *S* is depth in meters, *t* is time in nanoseconds and *V* is the the internal velocity of the signal through the medium. In this study, an average of three velocities (0,19 m/ns) evaluated by Håkansson in 2019 at Háabunga was used. This in an attempt to account for differing signal velocities throughout the stratigraphy due to presence of ash and varied rates compacted snow (see Figure 2.5 for details).

$$t = \frac{S}{V} \qquad (2.1)$$

Layer, n	Velocity $V\ (m/ns)$	Thickness $\tau\ (ns)$	TWT $t\ (m/ns)$
1	0.18267	30	60
2	0.16240	84	144
3	0.22723	140	284

Figure 2.5: *Table copied from Håkansson (2019) showing layer velocities, thicknesses and reflection time (TWT) within Vatnajökull as computed from a CMP Analysis in Háabunga. Ice (1) and (3), and the 2011 ash layer (2).*

Cumulative profile lengths were later calculated in Microsoft Excel using a three-dimensional distance equation (2.2) (Adams & Essex, 2014).

$$r = \sqrt{(x_2 - x_1)^2 + (y_2 - y_1)^2 + (z_2 - z_1)^2} \tag{2.2}$$

The equation determines the distance between each successive pair of points in three dimensions, then the cumulative distance along the profile was calculated using the SUM-function along columns (*Figure 2.6*). With both cumulative profile length and time depth determined, the profiles can be corrected for elevation using the *Static Correction* in ReflexW, enabling the possibility of visualizing the topographic differences important for the 3D-modeling.

When all profiles had been processed, their images were extracted to be further handled in Arcmap.

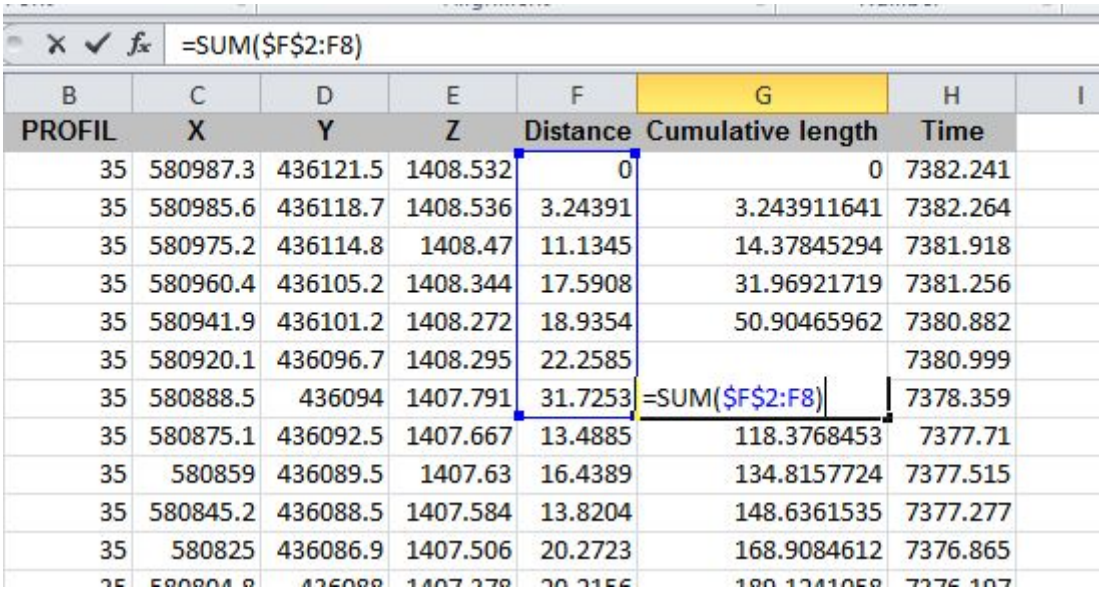

Figure 2.6: *Showing how the cumulative length was calculated from the distance equation in Excel. X-Y coordinates were extracted from the GPS, and the elevation retrieved from the DEM. Time was calculated with equation (2.1).*

2.4 Three-dimensional Modeling

The three-dimensional modeling required the use of several software packages (Microsoft Excel, ReflexW, ESRI ArcGIS Suite's ArcMap and ArcScene) and was partially aided by the step by step guide presented by Bergstrand and Johansson (2013).

2.4.1 Two-dimensional Plotting of GPR Reflections

After the GPR processing in ReflexW, the three-dimensional modeling of the layers required a process of two-dimensional plotting for each profile of the associated layers of interest. The GPR profile images and their associated reflectors of interest were georeferenced in Arcmap against a reference profile (profile 0015) containing the highest elevation point among all profiles (see *Figure. 2.7* for illustration). Reflectors of interest were identified within each profile, and then plotted using the *Create Feature (point)* function in ArcMap. The coordinate data was then calculated using the *Calculate Geometry* function before extraction. Additionally, a depth correction factor was calculated from the georeference values for each profile (see *Figures 2.7 & 2.8* for further explanation). (Bergstrand & Johansson, 2013)

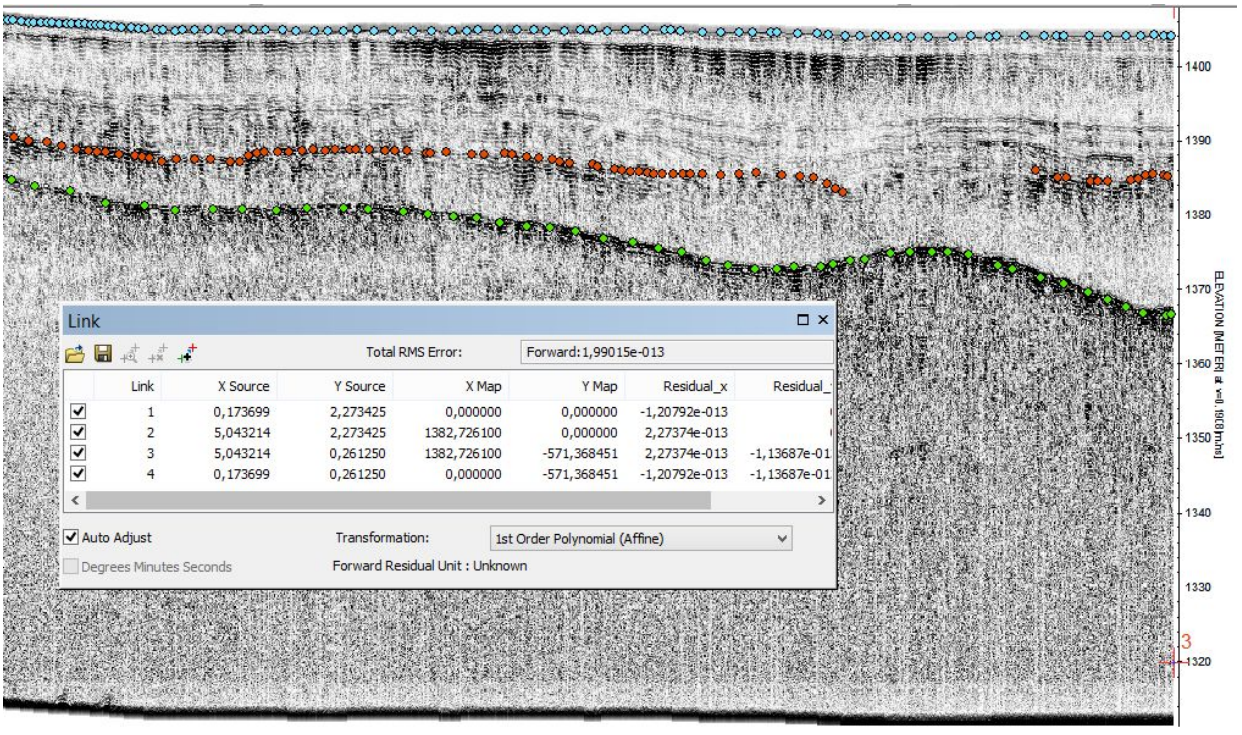

Figure 2.7: *Screenshot example of an ArcMap georeferencing Link Table (foreground), and the referenced GPR profile (profile 0006 example) in the background. Colored dots in the profile mapped along the reflectors of interest. The "X Map" coordinate point value in the table (Link 2 and 3) was typed in at the furthest extent (length) of the profile in meters. The default "Y Map" coordinate points (link 3 and 4) were kept in order to avoid distortion of the image during reflector mapping (Bergstrand and Johansson, 2013).This would later be corrected for using a depth correction constant (D_C) for each profile (see Figure 2.8 step 1.c for mathematical expression). Note that only the source ("X/Y Source") for the first link point was unanimous throughout all profiles.*

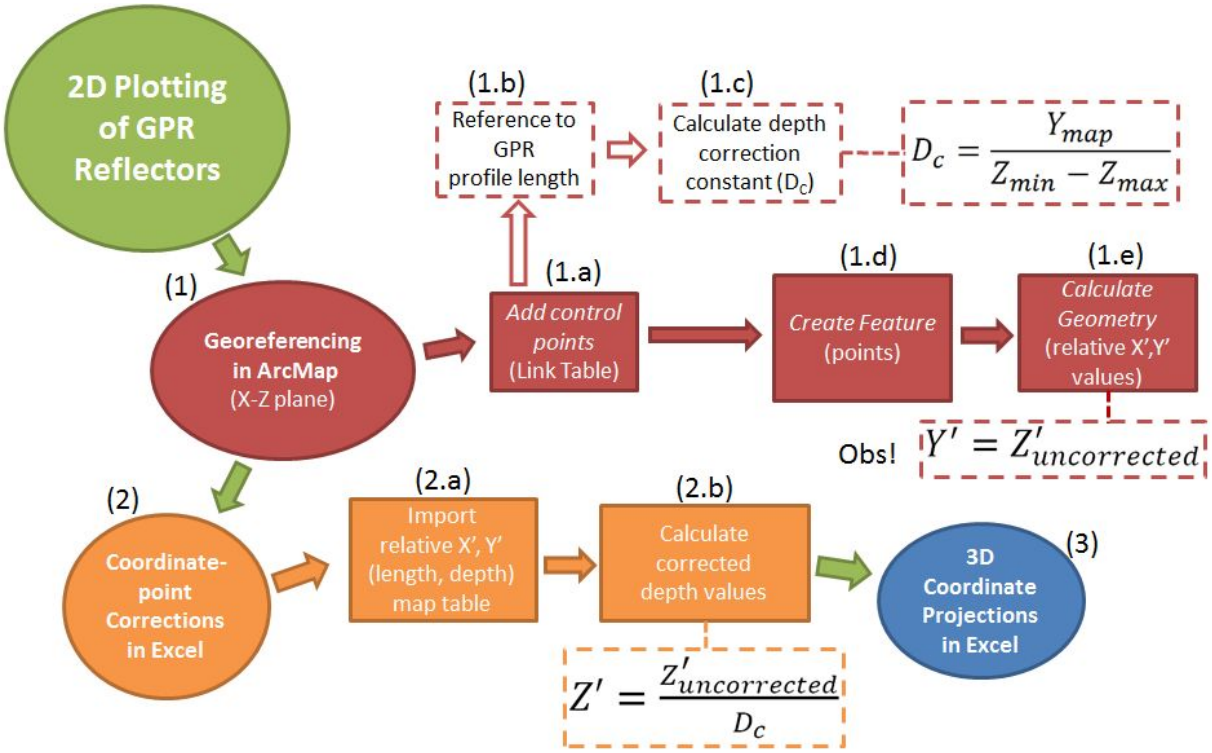

Figure 2.8: *Flow-chart of the two-dimensional plotting of the GPR reflectors (steps 1 and 2). Detailed workflow description of (1) Georeferencing in ArcMap, and (2) Coordinate point corrections in Excel. See section 2.4.2 below for step (3) "Coordinate Projections in Excel".*

2.4.2 Three-dimensional Coordinate Projections and Route Corrections

When the relative depths of each layer had been corrected, these were converted to absolute elevation values, but the geographical X- and Y-coordinates along the profile length had to be adjusted for their sidelong profile orientations. The angle was computed based on the coordinates from the profile offset and point of stop. The length of each profile layer was then projected using separate trigonometric functions, (see step 3.c in *Figure 2.9*) calculating for each X and Y coordinate value. Crooked and jointed profiles were roughly split into sections to account for the change of angle.

As each "flat" two-dimensional profile was projected along a theoretically straight line that did not align with the actual track route, the X-Y coordinates had to be further re-projected in ArcMap.

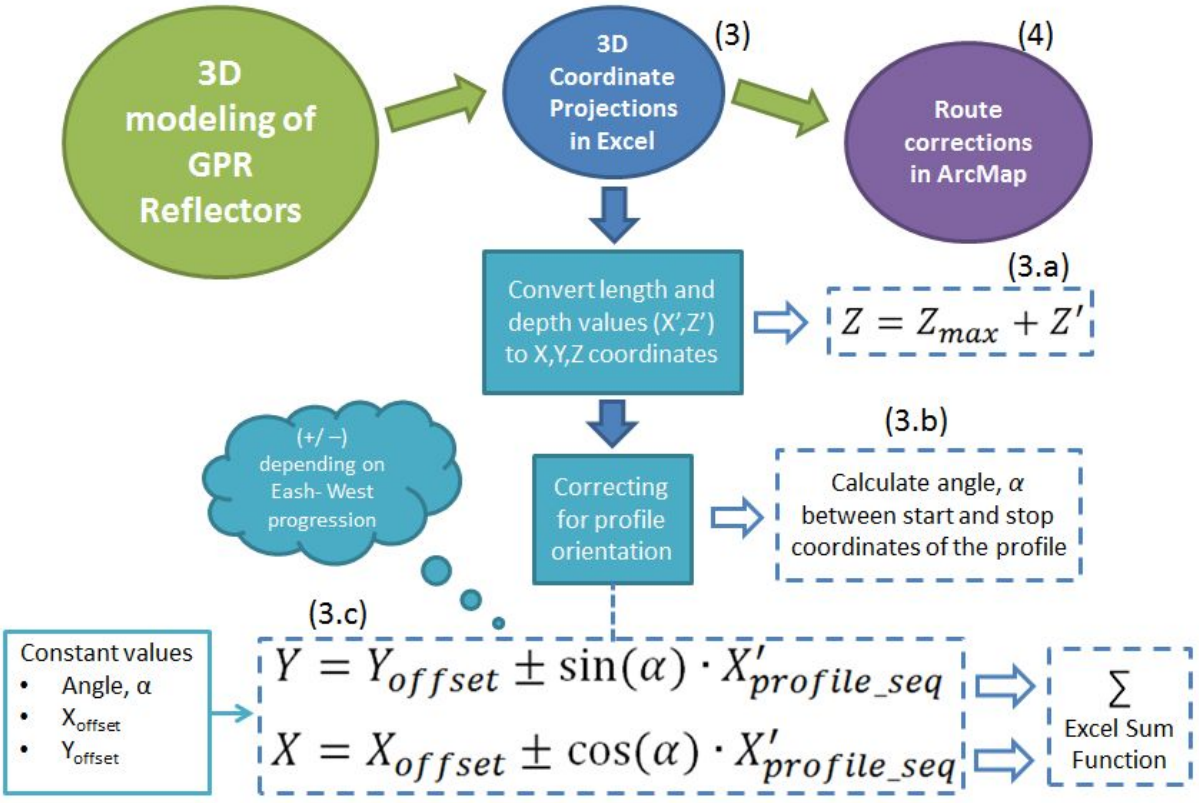

Figure 2.9: *Flow-chart of step 3, three-dimensional coordinate projections in Excel. In step 3.c noted in the figure, the trigonometric function was subtracted or added to the offset X- or Y-coordinate depending on the profile orientation angle between north-south and east-west axes. As shown in step 3.a, the relative (negative) depth values of each layer were simply added to the maximum elevation value of each profile.*

Before the GPR reflector surfaces could be integrated into a DEM from the layer coordinates, they had to be corrected for the GPS routing. This was done using the *Points to Line* tool in ArcMap (see *Figure 2.10*).

The plotted and projected reflector surfaces were then adjusted to plot along the line routes. This was done using the *Near* tool, (see *Figure 2.11*) which is a proximity analysis that calculates the nearest neighboring point on a line from a given feature class (ESRI, 2020). Subsequently each digitized GPR reflector layer was then re-plotted using the adjusted coordinate points.

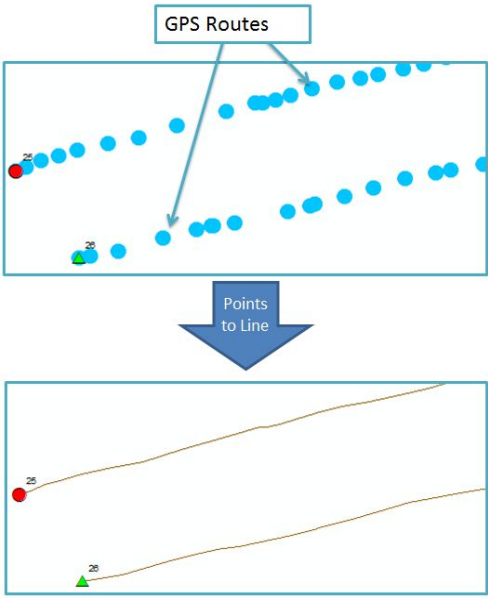

Figure 2.10: *Interstage of the route correction using the (ArcMap) Point to Line tool.*

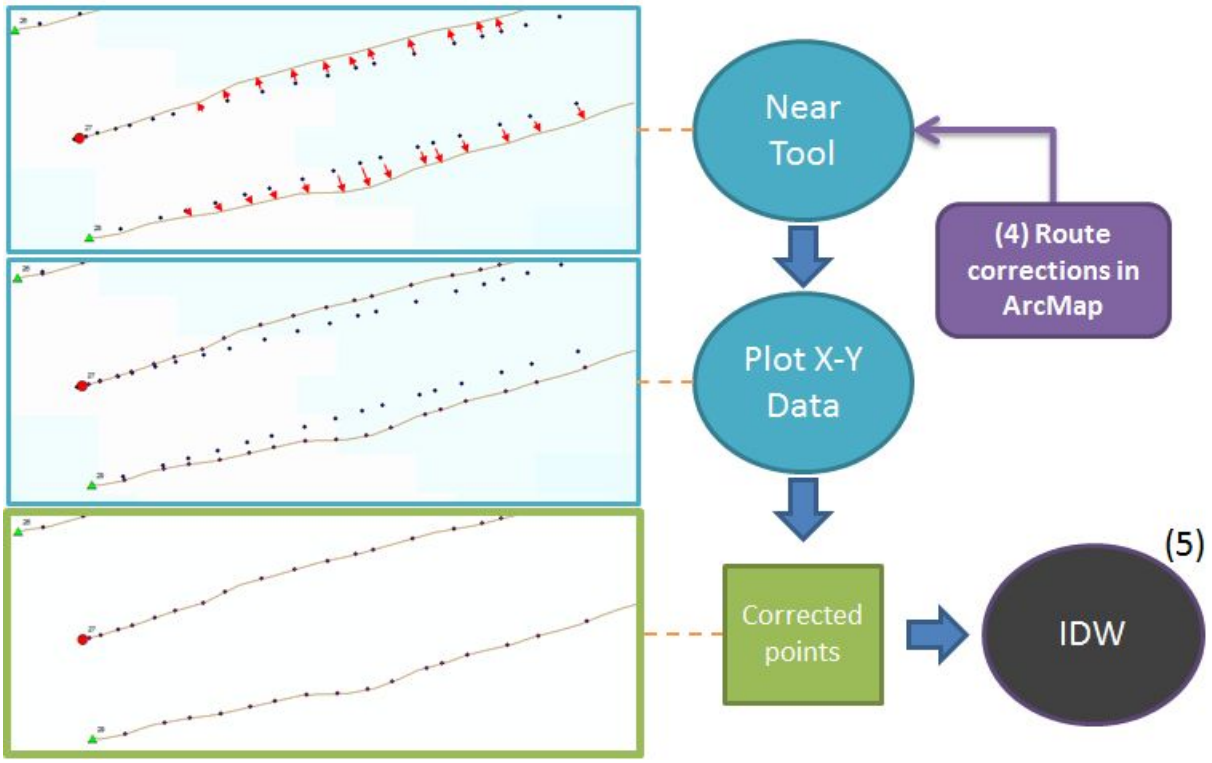

Figure 2.11: *Step (4) route correction in ArcMap. Demonstrating the proximity analysis and re-plotting of X-Y data before Inverse Distance Weighted (IDW) processing (step 5). Red arrows highlighting the route line of interest (top image). Note that the individual line routes and the projected coordinate points from the georeferenced 2D-profile layers needed to be worked separately in order for the proximity analysis to work properly.*

2.4.3 Surface Interpolation and 3D Plotting

Three-dimensional coordinate point clouds from the GPR reflectors were used to create three separate *Inverse Distance Weighted* (IDW) interpolations, producing one elevation raster for each layer. The IDW interpolation was done using a 'fixed' 1400 m distance (the furthest measured distance between two profiles) (Bergstrand & Johansson, 2013), with the lowest recommended power parameter (0,5) in order to smooth out the surfaces (ESRI, 2020). After the integration, the newly created DEM rasters were extracted (*Extract by Mask*) using a 500 meter buffer polygon (*Buffer* tool) around the merged line routes shown in *Figure 2.10* (above). See *Figure 2.12* (below) for workflow illustration.

The data layer was lastly plotted in ESRI ArcScene 10.5, which enabled an interactive 3D-navigation of the end results.

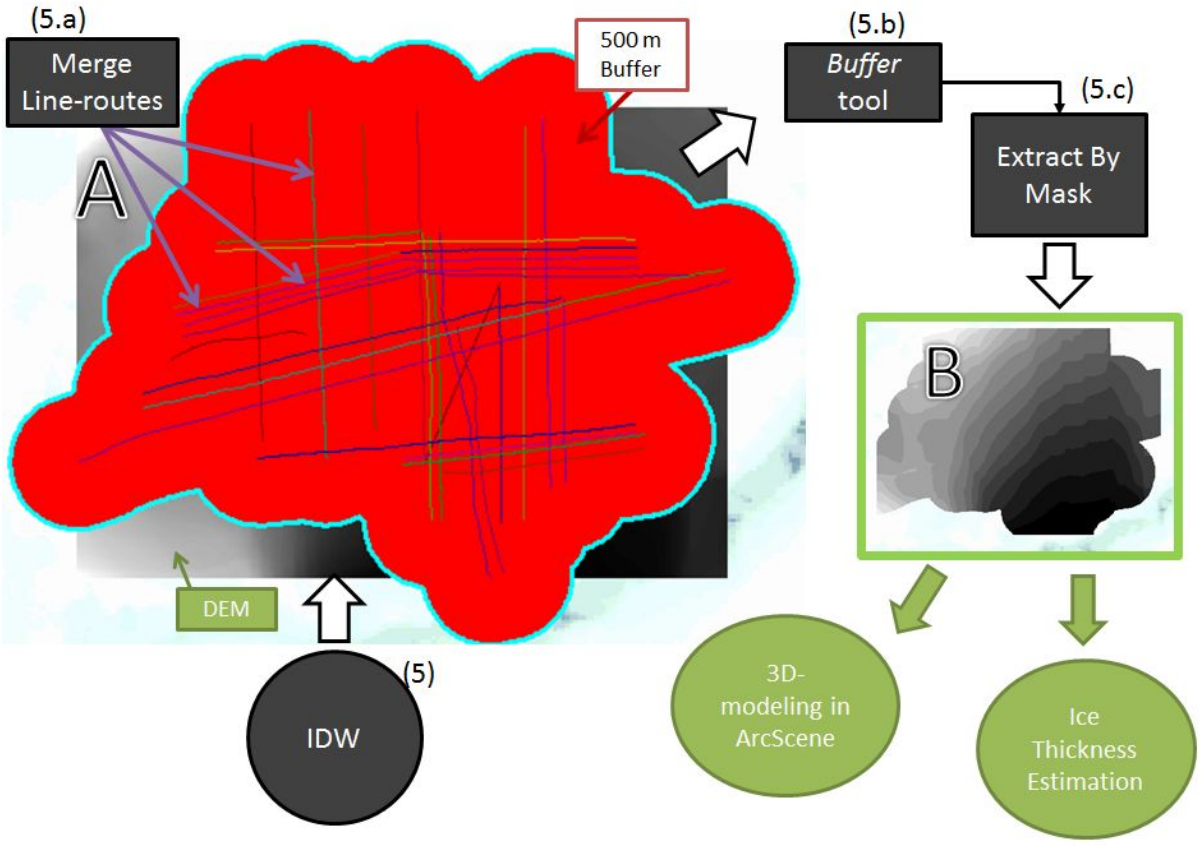

Figure 2.12: *(Step 4) IDW of GPR 3D coordinates. (A) 500 m buffer created from the merged line routes used to mask-extract the three elevation rasters. (B) Extracted DEM.*

2.5 Raster Calculations

A thickness estimation of the snow and ice between and above the two ash layers was done by subtracting the underlying layer elevation values from the one above it. To ensure the accuracy of the output raster (ESRI, 2019), the two term rasters to be subtracted had to be matched in both cell size and extent (steps 6.c and 6.d in *Figure 2.13*). The depth difference rasters were produced using the ArcMap *Raster Calculator* after having been extracted with the 500 m buffer mask created in step 5 of *Figure 2.12* (above). The resulting raster tables containing difference values were then exported to Excel (step 7 in *Figure 2.13*) where their mean thickness and a rough estimate average accumulation rate could be calculated (steps 7.b & c seen in the same figure).

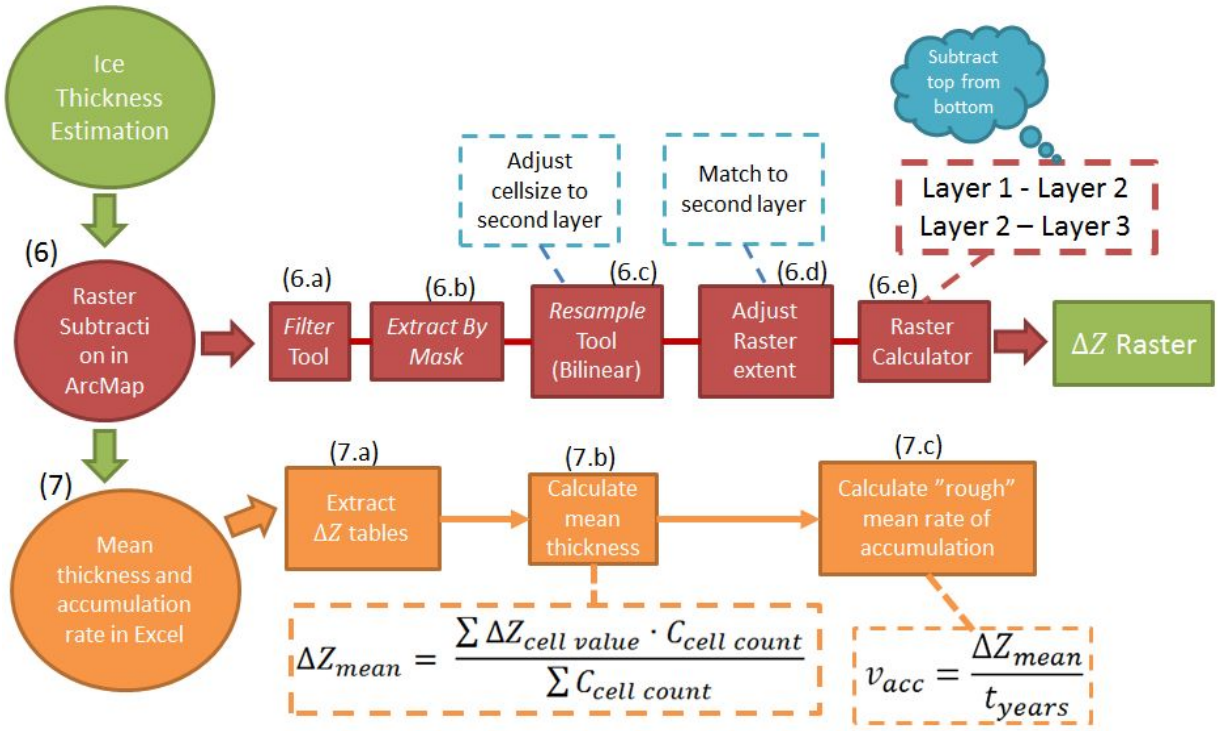

Figure 2.13: *(Steps 6 and 7) Raster subtraction in ArcMap, mean thickness and accumulation rate in Excel. Note that the accumulation rate equation (step 7.c) does not account for ice, snow and firn density changes due to compaction.*

2.6 Hyperbola Mapping

Fracture zones as interpreted from GPR hyperbolas were charted out by measuring the section lengths against the profile position in ArcMap.

3. Results

3.1 GPR Sections

Most of the GPR sections produced by the ReflexW software demonstrate uneven layer thicknesses and topography. In most sections you can clearly see strong reflectors as shown in the *Figure 3.1.* These are interpreted as the ash layers from the two most recent eruptions (2004 and 2011).

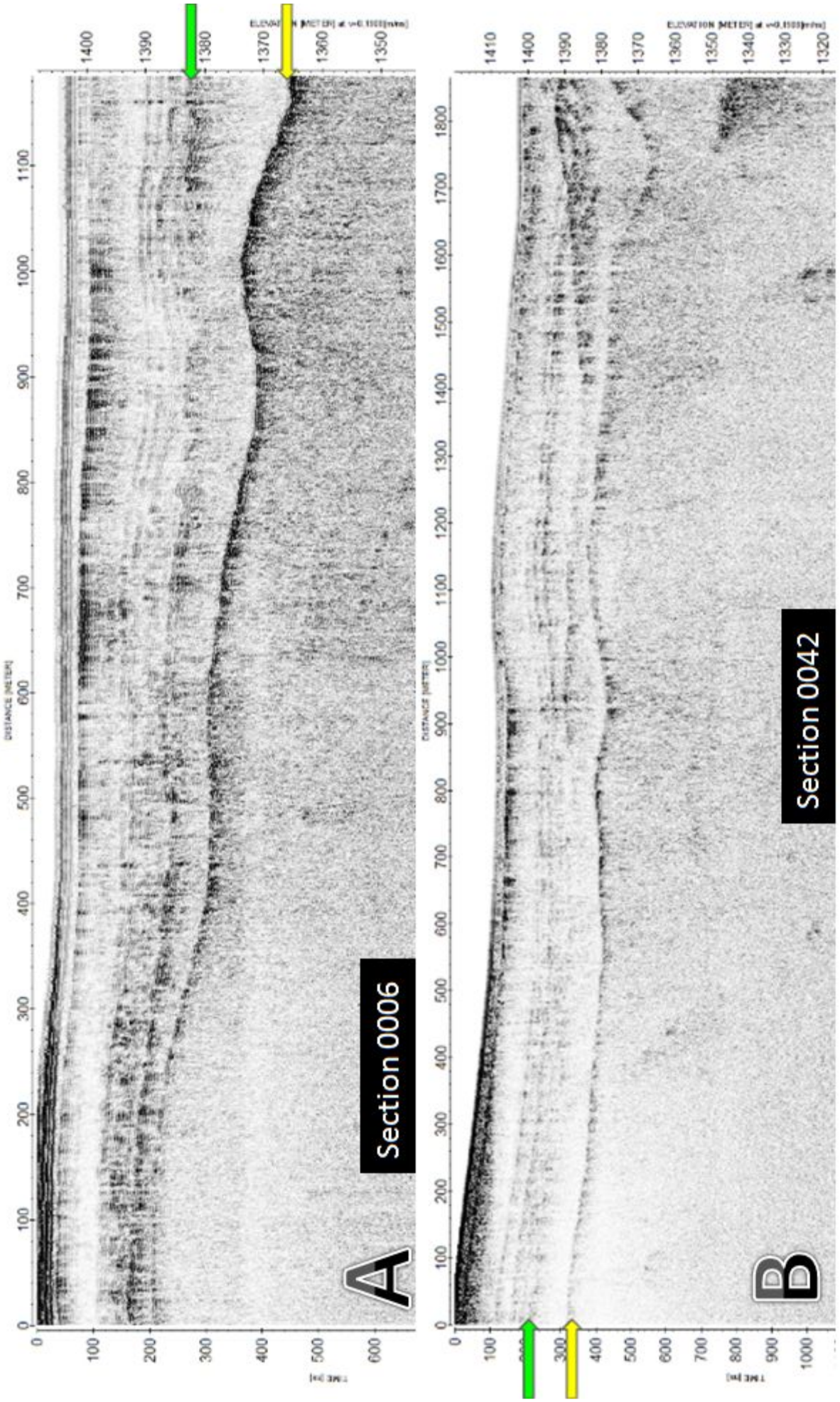

Figure 3.1: *Two of the sections. A) Ash layers from section 0006 with a N-S direction, and B) Ash layers from*

section 0042 with a W-E direction. Green and yellow arrows pointing to the mapped 2011 & 2004 ash layers respectively.

3.1.1 Indicative Reflectors and Hyperbolas

Indicative hyperbolas are seen in a majority of the sections. These are often associated with surface depressions in the topography. The hyperbolas seen in the ReflexW sections are interpreted as either fractures, meltwater tunnels or crevasses of different size and spread in the glacial ice (see *Figure 3.2* for example).

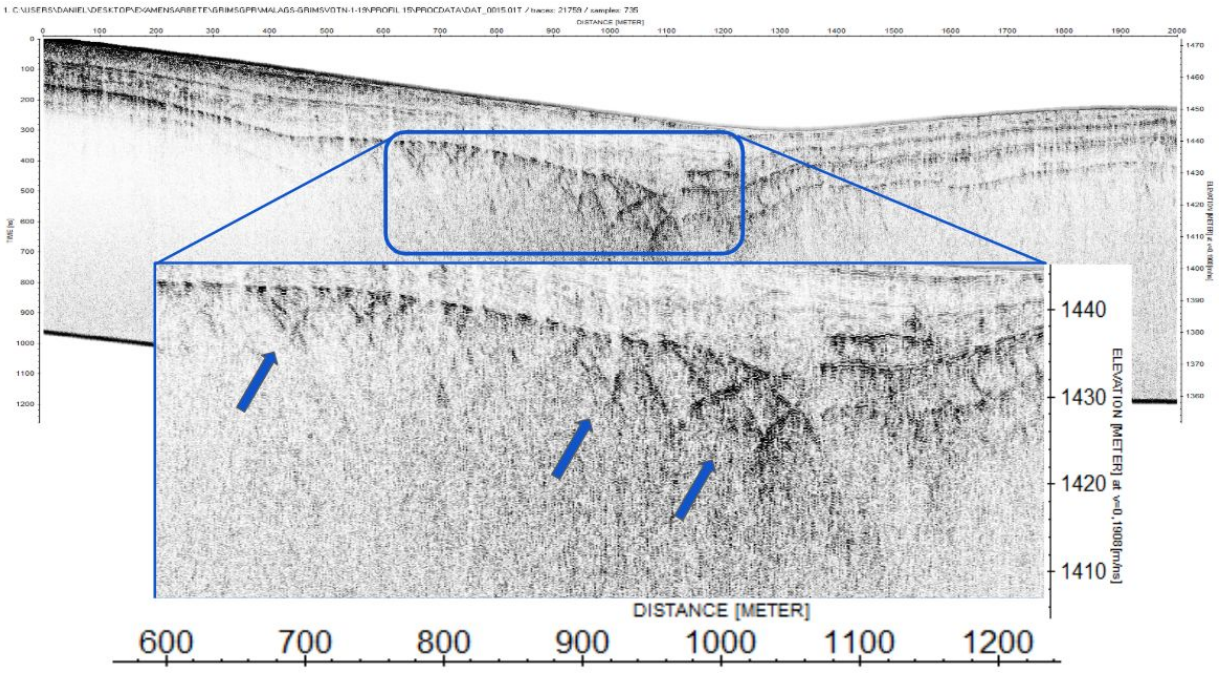

Figure 3.2: *Profile 0015. Blue arrows pointing to a few of the indicative hyperbolas seen in this GPR section. These are likely ash-filled fractures.*

The GPR profiles reveal many indicative hyperbolas that coincide in various groups and zones in the Grímsvötn area of Vatnajökull. The majority of the groups of hyperbolas are found along the southern rim of the crater, stretching in a SE-NW line, indicating a possible connection. Some of the mapped hyperbolas also gather around the north-east *(Figure 3.3*).

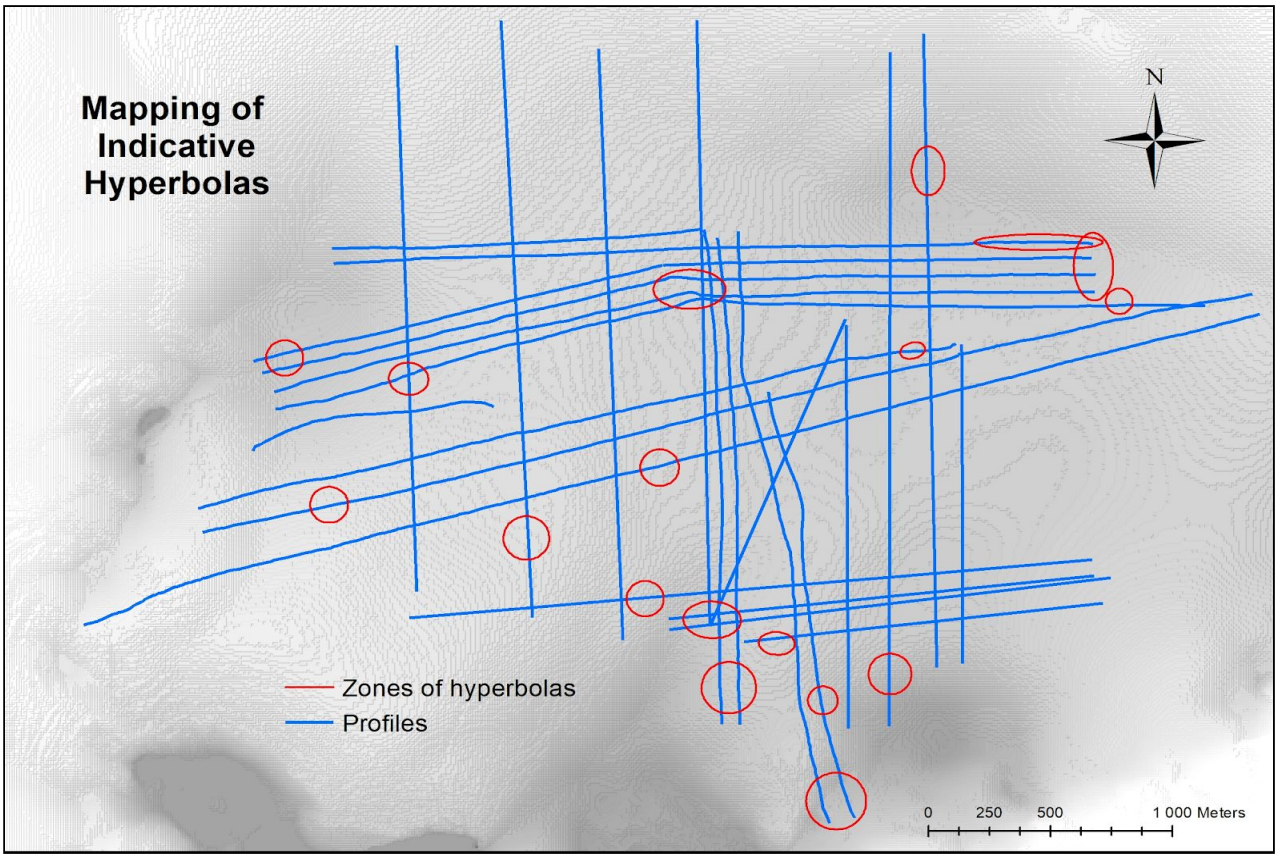

Figure 3.3: *Map showing zones of indicative hyperbolas interpreted from the GPR profiles across the Vatnajökull glacier. DEM background based on data from National Land Survey of Iceland (2016).*

The hyperbolas reflected in some GPR sections seem to be associated with an unevenness in the glacial surface. In *Figure 3.4* of profile 0008, a surface depression can be seen directly related to the hyperbola (a possible fracture or meltwater tunnel) at the bottom.

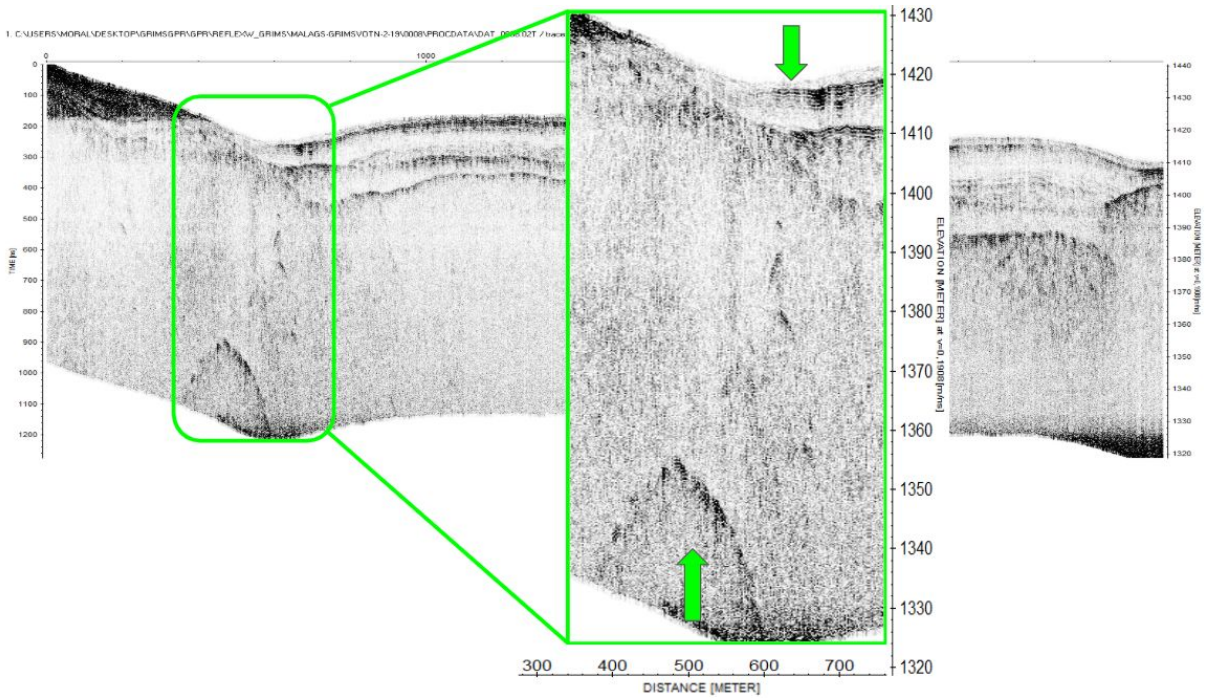

Figure 3.4: *Profile 0008. In this GPR section, a large hyperbola seems to be associated with the topographic depression in the surface. A main fracture or meltwater tunnel is likely found at the bottom.*

3.2 Three-dimensional Model

Georeferencing, mapping, plotting and interpolation of the reflectors interpreted from the processed GPR profile data resulted in a 3D model of three surfaces residing within the Vatnajökull ice.

The 3-D model consists of: (1) a surface layer interpreted as snow from the topmost reflector; (2) a mid-depth reflector believed to be an ash layer from the most recent volcanic eruption in 2011; and (3), a bottom layer interpreted as the volcanic ash layer from 2004. See *Figures 3.5, 3.6* and *3.7* for information snapshots of modeling results.

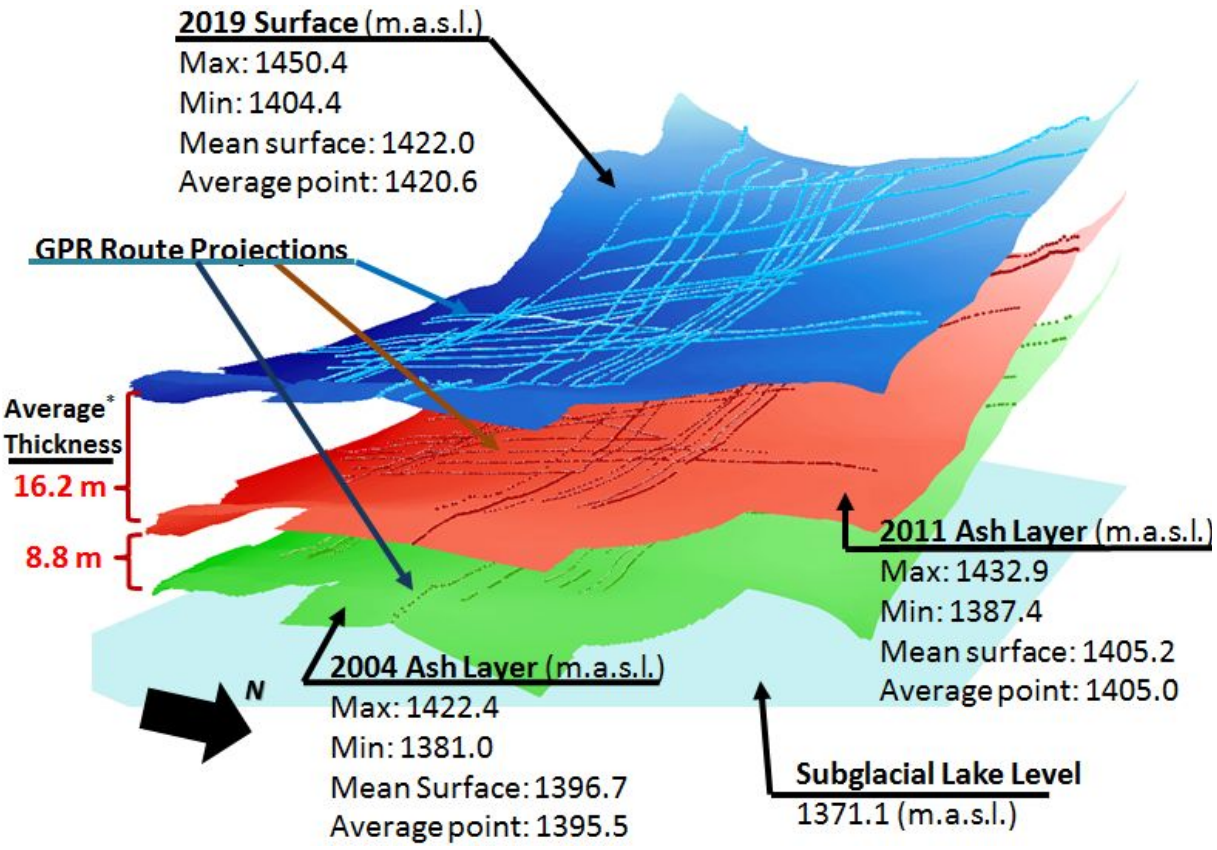

Figure 3.5: *Westward facing view of the 3D model from ArcScene (edited in Microsoft PowerPoint) showing all three layers mapped: Surface, 2011 Ash Layer and 2004 Ash Layer with their respective maximum, minimum and average elevation values. The elevation layers shown were extracted using the 500 m buffer mask of the DEM. Vertical exaggeration 30:1.*
**Average thickness calculated according to step 7.b in Figure 2.13.*

The top layer (*Surface)* has an average elevation of 1422.0 m.a.s.l. with its highest and lowest elevations located at 1450.4 and 1404.4 m.a.s.l. respectively. The lowest point of the surface is located at the south wall and is positioned 332 m below the summit at Háabunga (roughly 5 km away).

The mid-depth reflector (*2011-Ash* layer) rests at an average of 16.2 meters below the *Surface* and is positioned at 1405.2 m.a.s.l.

The lowest plotted reflector (here referred to as the *2004 Ash Laye*r) starts at its highest at 1422.4 m.a.s.l. and then slowly declines, stopping just 10 meters above the 2019 lake level at 1371.1 m.a.s.l. (see *Figure. 3.7*). This reflector has an average depth of 25.0 meters below the surface and is slanted toward the south-east in similar fashion to the layers above it.

The results from the GPR model reveal that the mapped reflector surfaces are all lowest toward the south wall of the caldera.

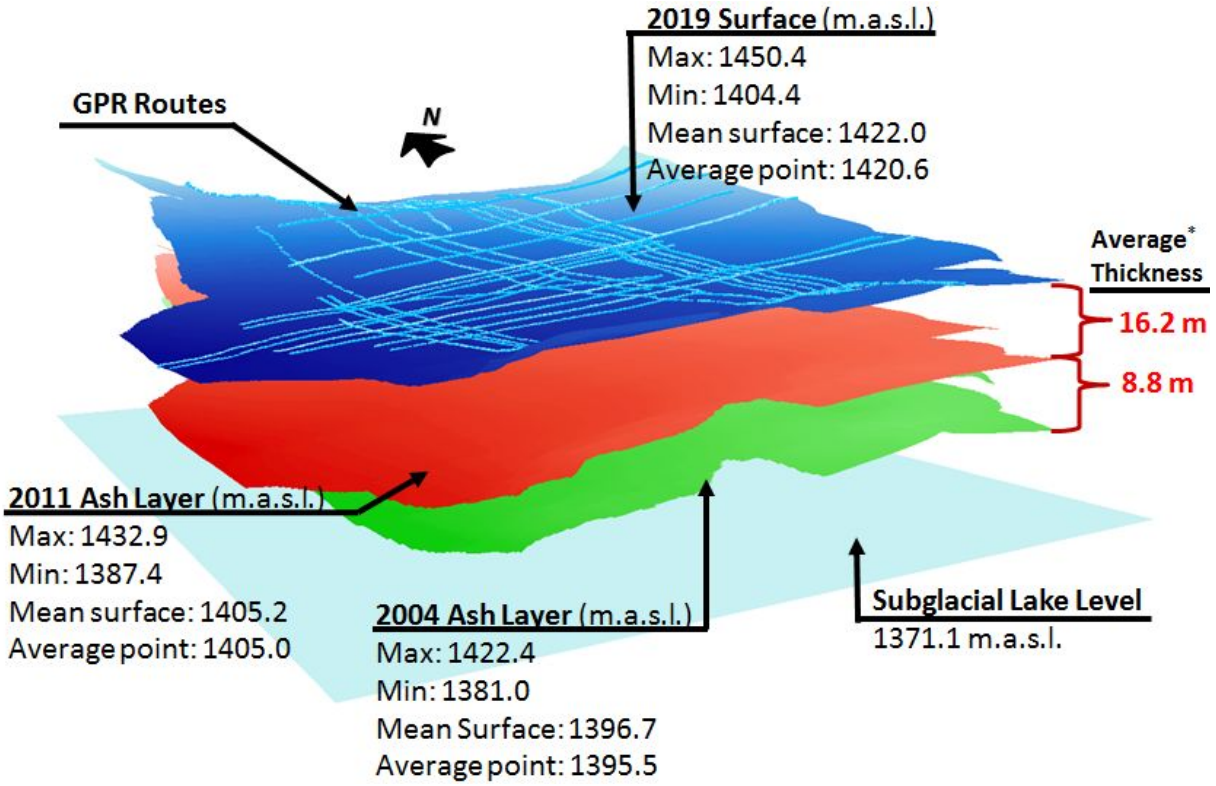

Figure 3.6: *North-east facing view of the 3D model in ArcScene (edited in Microsoft PowerPoint) showing all three layers mapped: Surface, 2011 Ash Layer and 2004 Ash Layer with their respective maximum, minimum and average elevation values.The elevation layers shown were extracted using the 500 m buffer mask of the DEM. Vertical exaggeration 20:1.*

**Average thickness calculated according to step 7.b in Figure 2.13.*

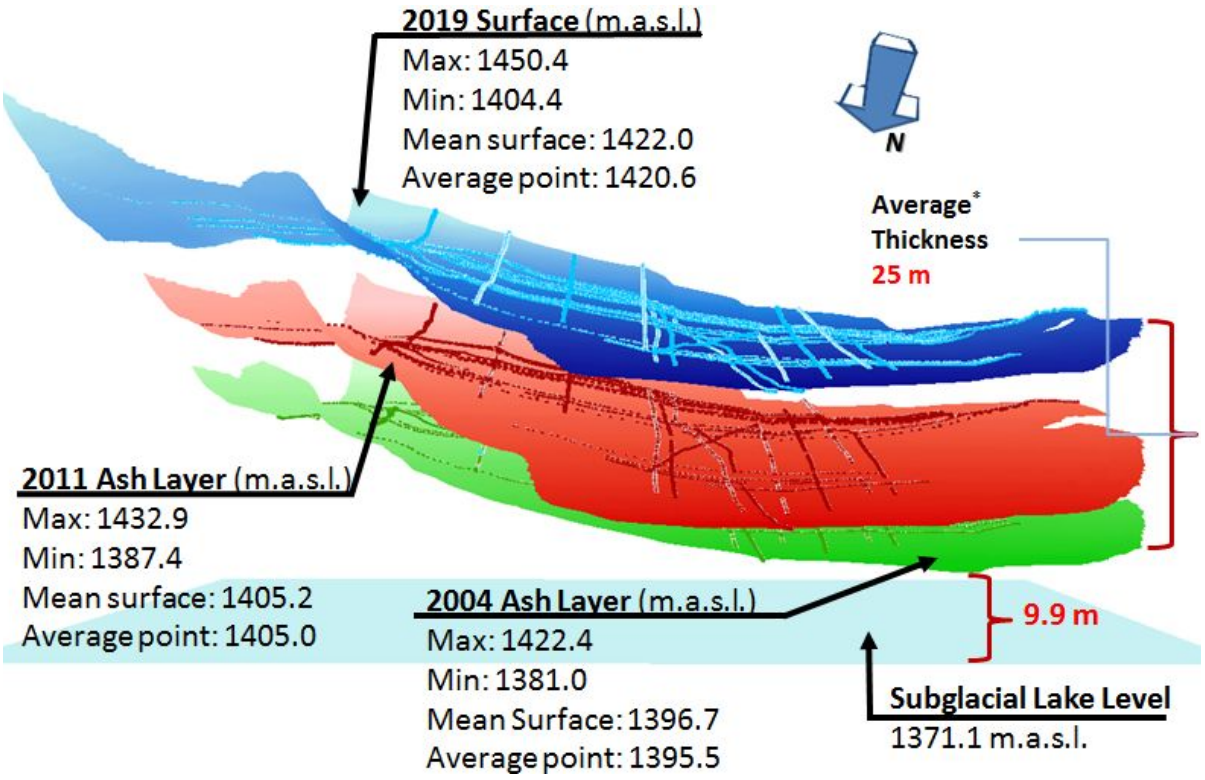

Figure 3.7: *North (side) view of the 3D model from ArcScene (edited in Microsoft PowerPoint), showing all three layers mapped: Surface, 2011 Ash Layer and 2004 Ash Layer with their respective maximum, minimum and average elevation values. 9.9 m is the minimum distance between the bottom 2004 Ash Layer and the subglacial lake at 1371 m.a.s.l. Elevation layers extracted using the 500 m buffer mask of the DEM. Vertical exaggeration 30:1.*

**Average thickness calculated according to step 7.b in Figure 2.13.*

3.3 Ice Thickness and Accumulation

Spatially, the thickness of the two ice sequences sandwiched between the three layers (*Surface*, *2011-Ash*, and *2004-Ash* layers) vary throughout the measured area, and they seem to follow different patterns. Between the *Surface* and the *2011-Ash*, the ash layer is buried deepest along the southern caldera wall (17-20 meters) and along the western and northern rims (16 to 20 meters), the exception being toward Naggur (at the surface section of the glacial lake) where the ash is expected closer to the surface.The shallowest areas, ranging between 13 and 15 meters, are found along a band stretching from the south-west near the lake to the north-east where it coincides with the appearance of hyperbolas found within the GPR profiles mentioned in section 3.1.1 (see *Figure 3.8*).

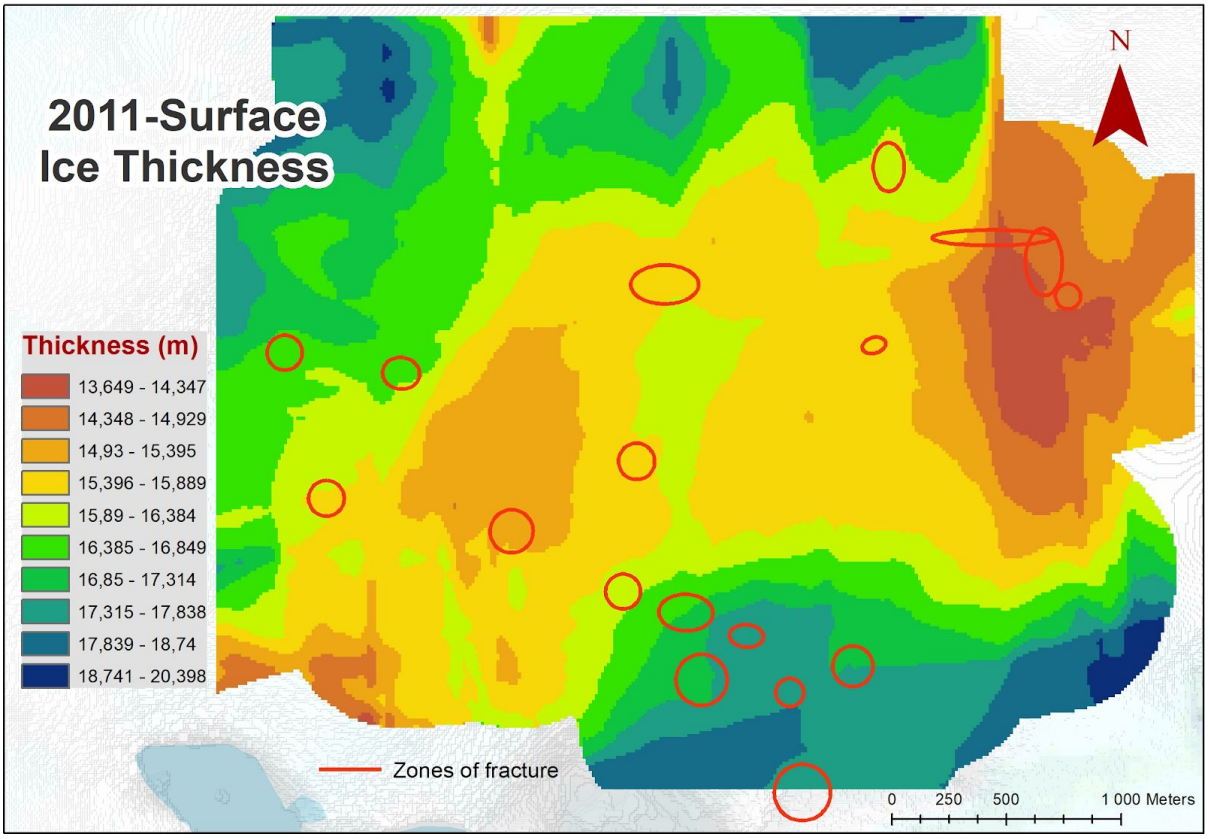

Figure 3.8: *Ice and snow thickness variation between the 2011 Ash Layer and the 2019 Surface. Results showing a low-value band stretching from the S-W toward the lake (light blue) to the N-E edge of of the sample area of the caldera. DEM background based on data from National Land Survey of Iceland (2016).*

The layer of ice and snow between the two ash beds (see *Figure 3.9*) reveals dissimilar thickness variations with a slightly wider span of values. In this sequence, the shallow areas show a dominating north-south facing trend reaching its shallowest at the southern margin of the caldera at roughly five meters from the layer above it. This is where the two ash layers are found closest together. This ridge is also dominated by a stretch of fracture zones presented earlier in section 3.1.1. On the westward side, closer to the caldera rim, the distance between the ash layers is larger (roughly 10-15 meters), with thickness values rising from south to north. This pattern is shared by both sections, as is the patterns of low thickness values seen at the center of the caldera.

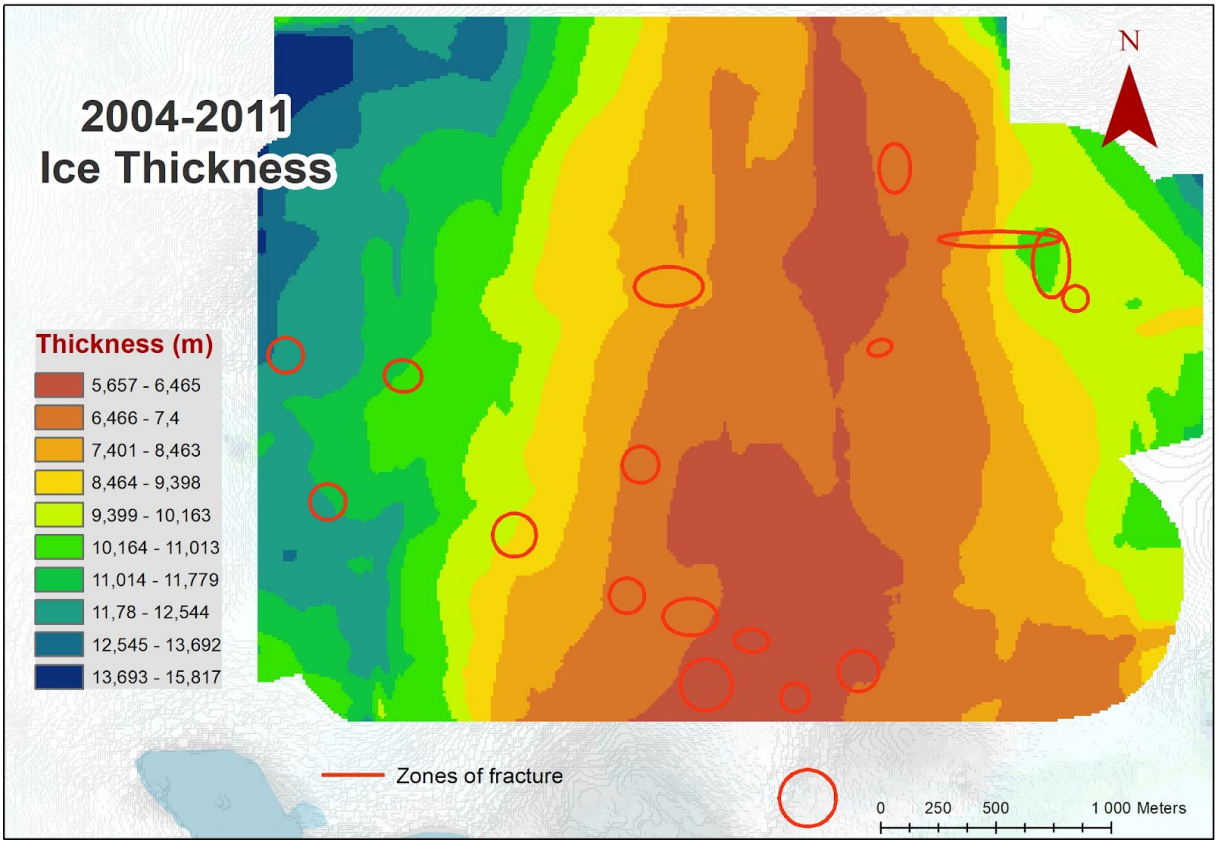

Figure 3.9: *Ice thickness variation between the 2004 and 2011 ash layers showing larger thicknesses in the west and east edges of the investigated site. Note the shallow thickness in the middle area stretching north to south. DEM background based on data from National Land Survey of Iceland (2016).*

The uppermost sequence (between *Surface* and *2011-Ash*) has a mean layer thickness of 16.2 meters with an estimated thickness accumulation of 2 m/year, (not accounting for the natural density effects due to compaction). The mean value of the bottom sequence is roughly half as thick, resulting in roughly half the rate of accumulation using the same method of estimate (see *Table 3.1*).

Table 3.1: *Mean layer thicknesses and thickness accumulation rates as calculated between the 2019 Surface and 2011 ash 2011 Ash layer, and between the two ash layers (2004 and 2011).*

Timespan	2011 - 2019	2004 - 2011
Number of Winter snows [years]	8	7
Mean layer thickness [m]	16.2	8.8
*Snow Thickness [m/year]	2.0	1.3
Comparison value [m/year]	**1.9	***N/A

**Calculation does not account for natural density effects due to compaction of snow, firn and ice.*
***The comparison value of the mean accumulation rate as reported by Håkansson (2019).*
**** No comparison was made for the 2004-2011 thickness due to absent 2004 ash layer in Håkansson's (2019) report.*

4. Discussion

The 3D model has allowed an estimate of the different layers of ash trapped in the ice cap stratigraphy, due to the Grímsvötn volcanic eruptions on two separate occasions. These are believed to be the remnants from the 2004 and 2011 volcanic eruptions.

4.1 Ash and Snow Accumulation

When comparing the results to the work done by Håkansson (2019), we realized that the ash layer from 2004 was not found in Háabunga, south of the caldera. The reason for this is most likely that the local winds in 2004 failed to facilitate enough deposition as it did later in 2011 where ash falls were driven over Háabunga south from the caldera (Smithsonian Institution, 2011).

4.1.1 Thickness variation of the Surface-Ash sequences

Mass movements such as avalanching and windblown snow strongly impact the local patterns of snow accumulation in glacial settings (Benn & Evans, 2013). Variations in wind speeds naturally affect the erosion of all windblown particles, be it snow or ash (Prothero & Schwab 2014). Such erosion may be governed by microclimate, affected by local wind and topography. The thicker ice pack observed above the 2011 ash layer at the southern edge could therefore be explained by a combination of added snow cover due to avalanching and snowfall wind trapping at the caldera rim. However, there may also be a shading effect caused by its position in the lee south caldera wall at Grímsfjäll, where it is likely more protected from the midday sun (see *Figure 4.1* below).

The density gradient between “snow”, “firn” and “glacial ice” of a glacier can not be expected to be constant or even linear (Benn & Evans 2013). It is therefore important to mention that snow and ice accumulation rates calculated by Håkansson (2019) and by these authors can *not* be considered an accurate estimate, and should only be referred to as comparison values for checking between results. In order to account for the compaction, a spatial model of ice densification would be required, the results of which could be translated into water equivalents.

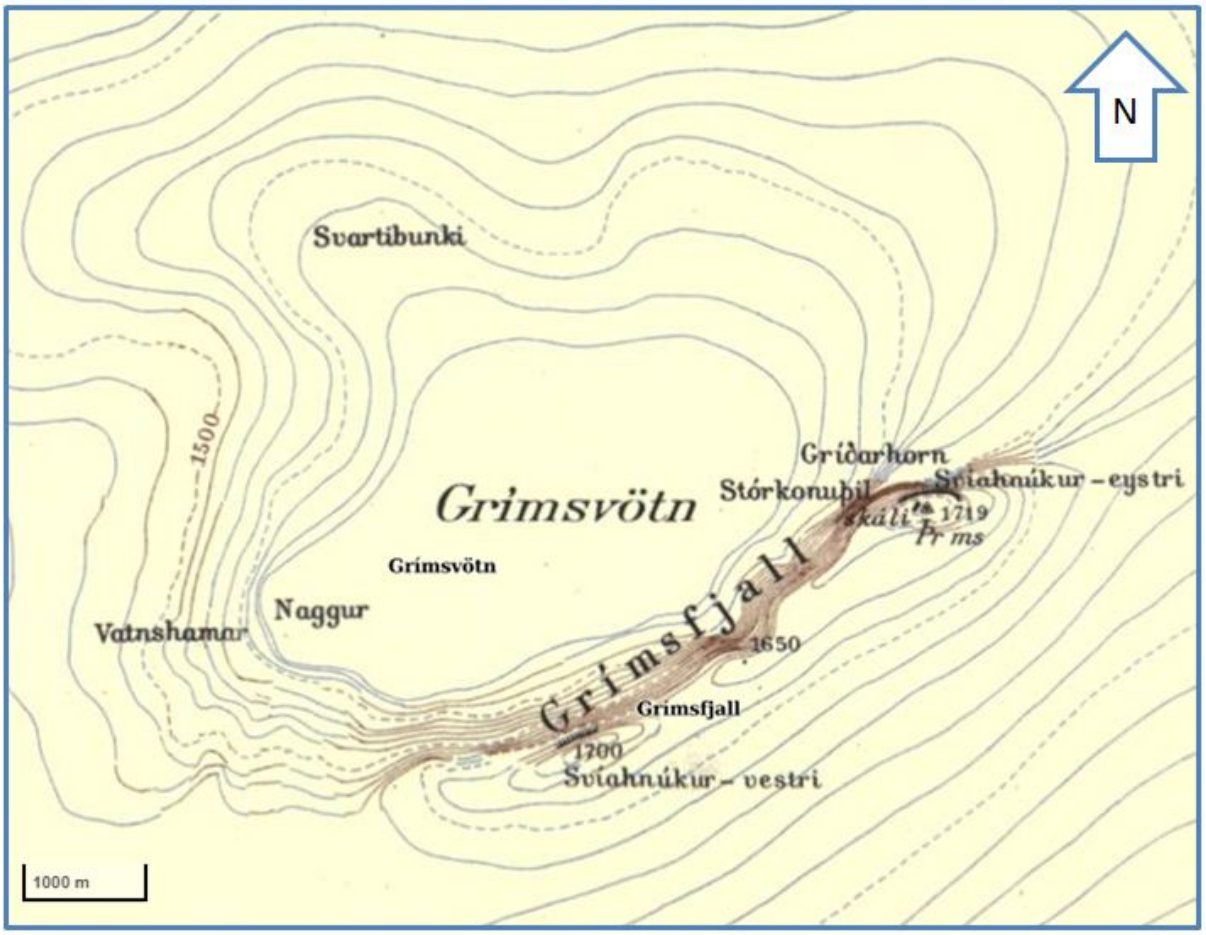

Figure 4.1: *Grímsvötn elevation variations based on data from National Land Survey of Iceland (2020).*

There are natural phenomenons other than simple weight compaction that may affect the rates at which snow is turned to ice (Benn & Evans, 2013), and many--if not all--of the conditions are met due to the placement and thermodynamic relationship between the Vatnajökull ice cap and the Grímsvötn caldera.

Melting and refreezing of surface snow is known to accelerate ice transformation. Percolating meltwater from the snow surface may have repeatedly permeated through snowpack pores and ice cracks, forming ice wedges and lenses deeper down where surrounding temperatures were low (Benn & Evans, 2013). Such findings were reported in the 2019 ice core data provided by Pálsson at the study area. This proposes that that the varied rates of accumulation and melting on the top of the ice may be in competition with the varying rates of melting at the bottom.

Decades worth of data has been recorded at Grímsvötn and is presented by Gudmundsson et. al. (2018) in a report covering discussions about the the heat flux and volcano-ice-interaction within the caldera. Their differential maps report that the ice shelf surface elevation varies greatly (up to +/-50 meters) from year to year and that it has a intimate connection to the subglacial lake levels. The same authors have

proposed that the thermal signals of post volcanic eruptions can be closely linked to geothermal peaks at the caldera walls.

Comparing the depth pattern of the top sequence to the one between the two ash layers we see that the southern side is by far the most shallow for the latter (see *Figures 3.8 and 3.9*). This could partially be explained by the fact that the topography of the caldera floor is tilted, and where the subglacial bedrock reaches its highest elevation toward the south at Naggur, volcanic activity (and therefore melting) is also at its greatest (Gudmundsson, 1989). Conversely, as the bedrock is located deeper further north heat flux exchange due to southside originating lava flows is also less pronounced (Gudmundsson, 1989), thus resulting in thicker ice.

The Vatnajökull ice is flowing toward the south and reaching annual top speeds up to 30 meters per year, a figure reported by Pálsson (personal communication, May 14th 2020), and as the ice drives toward the south caldera wall it sinks into the subglacial lake where it melts faster (Gudmundsson, 1989). The southward driving momentum of the ice may therefore be an added cause as to why the ice sequence below the 2011 ash layer is thinner in the south. As the ice compresses, driving into the warmer hydrothermal areas of the caldera, melting and compression may encourage the development of a southward facing slope, as has been observed in all three modeled layers. Furthermore, accumulating snow and ice from the caldera edges naturally add more to this compression. The relative magnitude and relevance of these effects however is unknown to these authors, and could be further investigated by other workers, comparing the glacial density gradient of the north and and south sections through the use of drilling and coring.

4.1.2 Effects of Superficial Debris

Superficial debris, whether or not caused by volcanic eruptions are factor that may significantly increase or lower the ablation rates of a glacier surface. These influences strongly depend on the debris layer thickness. While thin or patchy layers of surface tephra may increase the albedo, hence increasing the absorbed amount of shortwave radiation and melting at the surface, a thicker cover of debris may instead cause an insulating effect. (Benn & Evans 2013)

Assuming that the ash deposition would follow the same distribution patterns as the snow, one might expect the rise and fall of the ice layer thicknesses to be a function of the amount of overriding tephra. Further studies may discover if there is a correlation between the ash and ice thicknesses in the ice above Grímsvötn, and if so, how strong such a correlation might be.

Without historical ash thickness- and erosional data it is difficult (if not impossible) to determine with any degree of certainty which surface areas of the caldera may have been more dominated by the albedo or the insulation effect, especially in a temporal perspective, where spatial distribution changes are strongly affected by wind erosion. Further study of ash and ice thicknesses and density might help to answer this question, making use of multiple ice coring sequences to correlate between. However, such an investigation would undoubtedly be very costly. Drilling would also enhance the risks of upsetting the exotic subglacial ecosystem dwelling within the melted section of the caldera (Benn & Evans, 2013).

4.2 Glacial Tectonics

In some cases, surface depressions on the glacier seem to indicate stability problems within the ice above the caldera. These depressions are associated with a number of sharp hyperbolas identified as ash-filled fractures, meltwater tunnels or vertical ice glands within the ice (see example in *Figure 3.2*).

Interpretations of hyperbolas differ from interpretations made by Håkansson (2019) where these are related to crevasses and tunnels of larger magnitude. The hyperbolas shape in Håkanssons work are rounded at the top of the hyperbola and not as sharp as the hyperbolas found in the GPR sections from Grímsvötn.
There are sectors in Vatnajökull with a higher concentration of fractures and crevasses than others, and they are more prone to show deformations. Fracture mapping of southern profile sections (*Figure 3.7*) also match those found by Sturkell (personal communication, April 2020), who reported visible ice fractures along the southern parts of the caldera (*Figure 4.2*).

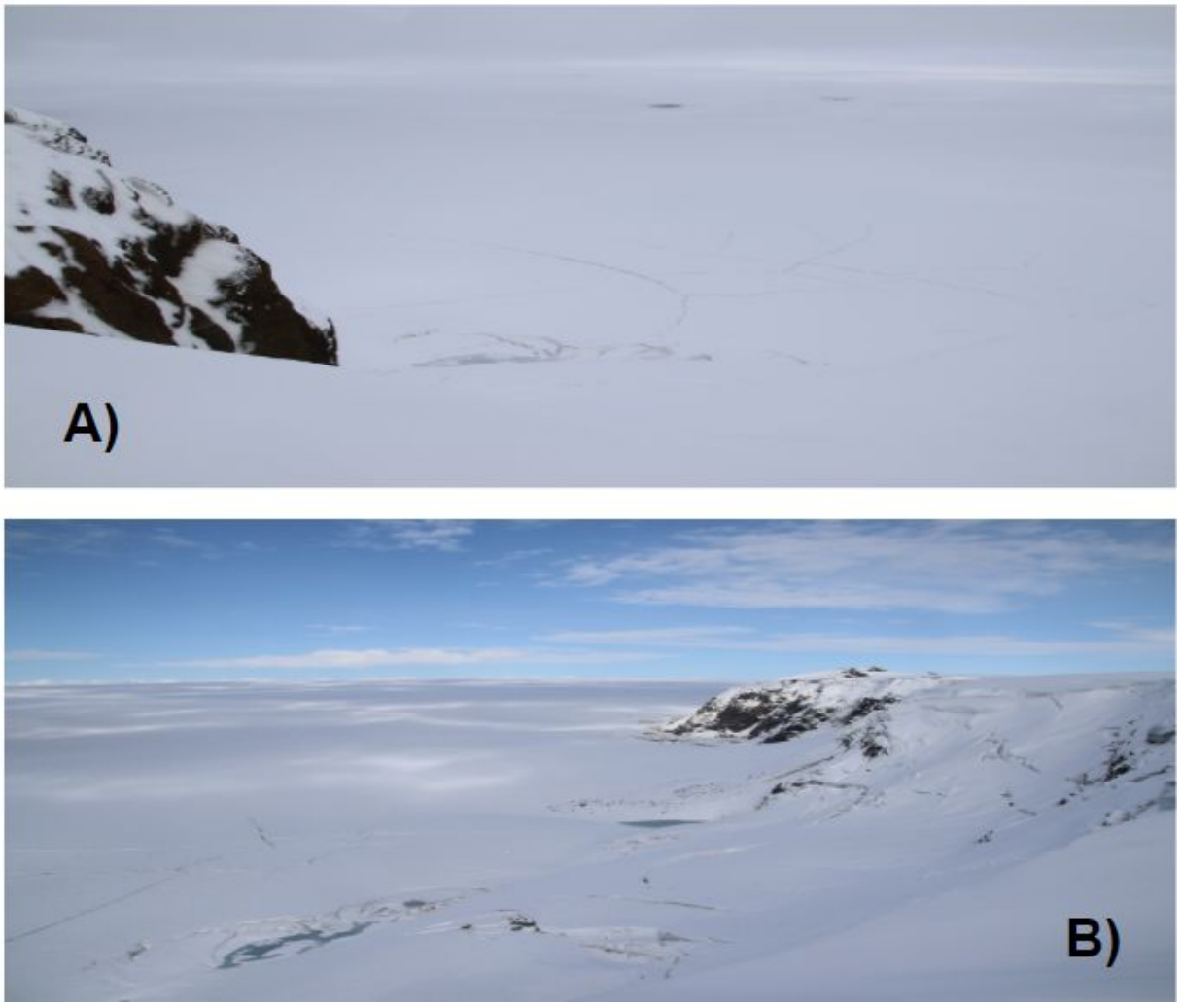

Figure 4.2: *The pictures A and B show the fractures zone in the ice cap surface at west of Svíanhnúkur (see Figure 4.1 for the site of Svíahnúkur-vestri). Photographs courtesy of Erik Sturkell (2020).*

As mentioned in section 3.1.1, the hyperbolas are located along the 2011 ash layer (see *Figure 3.2*) which may have been created shortly after the eruption, since the ice layer above it does not show alterations due to these fractures. Some of these could be relics associated to the kilometer long E-W facing fissure that was formed during the 2011 eruption, reportedly located in the south-eastern section of the caldera (Global Volcanism Program, 2011).

Fractures identified within the glacier may however not only be caused due to eruptions, but also be associated with the previously discussed geothermal energy supplied from the bottom of the caldera, (Björnsson, 2003; Benn & Evans, 2013). Continued basal melting may cause upwelling and induce fractures related to the deformation of the glacier surface (Benn & Evans, 2013). This is believed to be the case witnessed in *Figure 3.4*, where the surface depression seems to have a direct relationship with the fracture or meltwater tunnel at the bottom.

Dramatic alterations within the layer topography are most likely not only due to the fractured ice below it but also an effect of surface melting. Some sectors of the ice

cap were more affected than others, producing different relief along the former surface. This may be due to the albedo effect, caused by surface tephra as discussed in 4.1.2.

4.3 The Subglacial Lake Interface

The subglacial and subaerial lake at 1371 m.a.s.l. is not believed to have been close to the same level as the ice bottom interface. As long as the ice stays afloat the glacier and the lake undoubtedly stay at static equilibrium according to Pascal's principle (Cengel, Cimbala & Turner, 2008). The massive weight of the glacier most likely serves as a hydraulic lift against the lake and the true bottom of the ice is therefore located much deeper. Indicative hyperbolas of *something* were however seen far below the level of the lake at 1300 m.a.s.l. in many of the GPR profiles, but due to time restrictions, these could not be studied further. Whether this is the bottom of the ice or ash from the 1998 eruption remains an unanswered question. Such investigations are left to future workers that may be able to distinguish something of interest using different ReflexW settings.

4.4 The 3D Model and Sources of Error

As mentioned in section 2.2 there was a loss of differential GPS data along many of the N-S facing profiles (0006 to 0015). This resulted in straight line projections created between the start and end points of these profiles, causing the elevation parameters to be affected when when they were later cut out of the Iceland DEM. Including this error in the model influences the rest of the results acquired in Arcmap, Excel and ReflexW. Ultimately the IDW interpolation of all the elevation points extracted from all the combined profiles was likely affected in that, when including these straight profiles (not following their real path and not crossing with the real intersection points between the profiles) it raises and/or lowers the height of the interpolation both for the west and east side of the caldera.

As it is impossible to determine how greatly the true navigation deviated from the straight course between start and stop it is difficult to say how large an error was created by including these profiles, but it seems likely to believe that the difference in elevation caused by this error is not so great that an altered decision would have resulted in a wildly different interpretation of the data. However, after the modeling of the layers in ArcScene it was discovered that there were differences in the height of some of the crossing profile points. Something that should not have happened because the coordinates match and the heights are correct in the profile attribute tables, but could however be explained by the inclusion of the non-accurate profiles (0006 to 0015). Another reason as to why this may have failed could be that, during the georeferencing process, every profile was georeferenced against the profile containing the highest elevational value, which happened to be one of the non-accurate profiles (0015) and therefore there may have been a false offset,

affecting the point positions and interpolation of the points created from these sections.

Another error that may have altered our results is that we sometimes had to accommodate the start and end points on our own, since the given coordinates of these points did not match the points revealed by GPR along each profile. The readjustment of these points would result in a possible distortion between the real length distances of the profiles and the length distances in the model, but since the points were moved only a few meters at most this should not have affected the results to any great extent.

Using the ice core data provided by Pálsson to follow the tephra layers during georeferencing might have provided a more accurate interpretation as to the real elevation of the ash layers, thus decreasing the amount of deflection between the profiles in the results. However, because the ice core data was provided too late in the work process, correlation between the tephra found in the ice core and those interpreted from the GPR in this report was regretfully not possible. Furthermore, the ice core happened to be taken along one of the profiles without accurate GPS navigation data, which ultimately might have led to more of the same problems just discussed.

The decision to use an average of the velocities found at Håkanssons (2019) for all sections in ReflexW may have affected the differentiation of the reflectors, causing a small inaccuracy in the interpretation of the elevation of the layers and others features, found in the GPR sections. Using the different velocities for each layer the image could have produced a better estimate of the elevation values, although is difficult to say how much this would have affected the final results. A CMP within the caldera itself may possibly have been a great help in differentiating the layers more accurately within the caldera ice.

The model is nevertheless a possible tool for the interpretation of the layers of ashes in Vatnajökull as it no doubt shows the relative patterns of deposition within the caldera. And the results presented in this report are not believed to be far from reality.

5. Conclusions

This study confirms the reports from Håkansson (2019) that the 2011 ash layer varies in depth. It also adds to this observation that that the same can be said for the reflector seen at 25 meters below the surface (average in 2019) which has been interpreted as the 2004 ash layer. These two stratigraphic features will will hopefully serve as good chronostratigraphic markers in the future.

The opposing effects of albedo and insolation, alongside density effects caused by compaction, ice fracturing and meltwater infiltration and refreezing make for a difficult interpretation of the ice thickness data. However, the observations presented here clearly indicate a dramatic difference seen in the thickness patterns compared between the two sections. Top layer thicknesses are larger at the caldera edges, indicating a relatively higher amount of accumulation (the area near the lake being the exception). The surface is also seen to be thinner toward the center, most possibly due to a combination of distance from the accumulation zones at the rim and the surface effects of melting due to surface heating. Bottom layers show similar signs of accumulation along the western rim, as well as a thinner center, but ice thicknesses continue to thin out toward the southern caldera wall. This is believed to be a combined result of compression due to ice overburden and the momentum of Vatnajökulls continuous southward movements into the southward melting zone. Furthermore, basal melting due to thermal heat flux at the ice bottom is believed to have had heavy influence on the ice geometry and varying density. Results from the GPR hyperbola mapping reveal that there are a multitude of fracture zones likely associated with the thinning sections of the two ice sequences between the layers.

Summarizing, the Vatnajökull ice sheet above Grímsvötn is likely melting at different rates both along the top surface and the bottom. Further investigation of glacial density and tephra thicknesses is required in order to determine however the albedo effect or the insulating effect has been the dominating factor at the surface.

The work presented in this article was the result of a highly empirical process of iterative failing and learning. As many of the problems encountered with the 3D modeling had not been solved in the previous literature at hand, the authors were driven to experiment and reinvent a methodology through efforts of trial and error. These efforts resulted in a methodology which hopefully may be of use to future 3D modeling aspirants of seismic- or GPR profiles.

References

Adams, R. A., & Essex, C. (2014). *Calculus: a complete course* (8. ed.). Canada: Pearson

Benn, D.A., & Evans, D.J.A. (2013). *Glaciers & Glaciation* (2. ed.). New York: Routledge.

Bergstrand, C., & Johansson, J. (2013). *Presentation of Marine Geological Hydroacoustic Investigations in Kalmarsund, Sweden.* (Degree project, University of Gothenburg, Gothenburg)

Björnsson, H. (2003). Subglacial lakes in Iceland. *Global and Planetary Change, 35*(3), 255-271. 10.1016/S0921-8181(02)00130-3.

Cengel, Y. A., Cimbala, J. M. & Turner, R. H. (2008). *Fundamentals of Thermal-fluid Sciences* (4 ed.). Singapore: McGraw-Hill Higher Education.

Environmental Systems Research Institute (ESRI) (n.d.). Proximity Analysis. Retrieved 2020-05-07 from:https://desktop.arcgis.com/en/arcmap/10.3/analyze/commonly-used-tools/proximity-analysis.htm

Environmental Systems Research Institute (ESRI) (n.d.). How IDW works. Retrieved 2020-05-07 from https://desktop.arcgis.com/en/arcmap/10.3/tools/3d-analyst-toolbox/how-idw-works.htm

Environmental Systems Research Institute (ESRI) (2019). How To: Find raster value differences between two rasters in ArcMap. Retrieved 2020-05-07 from: https://support.esri.com/en/technical-article/000012806

Global Volcanism Program. (2011). Report on Grímsvötn (Iceland). Retrieved 2020-05-14 from: https://volcano.si.edu/volcano.cfm?vn=373010

Gudmundsson, M. T., Högnadóttir, T., Pálsson, F., Reynolds, H. I. (2018). *Journal of Volcanology and Geothermal Research, 358,* 184-193. https://doi.org/10.1016/j.jvolgeores.2018.04.019

Gudmundsson, M.T. (1989) The Grímsvötn Caldera, Vatnajökull: Subglacial Topography and Structure of Caldera Infill. *Jökull,* (39), 1-17.

Guideline Geo. (2011) MALA-RTA-Antennas. Retrieved 2020-05-15 from: https://www.guidelinegeo.com/wp-content/uploads/2016/03/MALA-RTA-Antennas.pdf

Háskóli Íslands, Institute of Earth Sciences. (n.d.). Eruption at Grímsvötn Volcano, 1 - 6 November 2004. Retrieved 2020-05-14 from: https://earthice.hi.is/eruption_Grímsvötn_volcano_1_6_november_2004

Háskóli Íslands, Institute of Earth Sciences. (n.d.). Grímsvötn eruption 2011. Retrieved 2020-05-14 from: https://earthice.hi.is/Grímsvötn_eruption_2011

Håkansson, A (2019). *Ash distribution and cavities in Icelandic glaciers, a marker for snow accumulation and radar signal velocity change.* (Master's thesis, University of Gothenburg, Gothenburg)

Jol, H. M. (Ed.). (2008). Ground penetrating radar theory and applications. elsevier.

National Aeronautics and Space Administration (NASA). (2004). Ash from Grímsvötn Volcano on Iceland's Vatnajokull. Retrieved 2020-05-07 from: https://earthobservatory.nasa.gov/images/5004/ash-from-Grímsvötn-volcano-on-icelands-vatnajokull

National Aeronautics and Space Administration (NASA). (2011). Eruption of Grímsvötn Volcano, Iceland. Retrieved 2020-05-07 from: https://earthobservatory.nasa.gov/images/50684/eruption-of-Grímsvötn-volcano-iceland

National Aeronautics and Space Administration (NASA). (2011). Eruption of Grímsvötn Volcano, Iceland. Retrieved 2020-05-07 from: https://earthobservatory.nasa.gov/images/51156/eruption-of-Grímsvötn-volcano-iceland

National Aeronautics and Space Administration (NASA). (2011). Grímsvötn Volcano Injects Ash into the Stratosphere. Retrieved 2020-05-07 from: https://earthobservatory.nasa.gov/images/50722/Grímsvötn-volcano-injects-ash-into-the-stratosphere

National Land Survey of Iceland (NLSI) (2016). *LMI Digital Elevation Model* [Data set]. Retrieved from: https://atlas.lmi.is/LmiData/index.php?id=1115579409382

National Land Survey of Iceland (NLSI). (2020). Map Viewer. Retrieved 2020-05-14 from: https://kortasja.lmi.is/en/

Oddsson B. (2007). *The Grímsvötn Eruption in 2004: Dispersal and Total Mass of Tephra and Comparison with Plume Transport Models.* Master degree in the Faculty of Science, Department of Physics, University of Iceland.

Pálsson, F. (2019). *Borth-2019.* Unpublished manuscript. Retrieved 2020-08-2020.

Petersen G. N., von Löwis S., Brooks B., Groves J., Mobbs S. (2012). Utilising a LIDAR to detect volcanic ash in the near-field. Royal Meteorological Society. DOI: 10.1002/wea.1891 https://rmets.onlinelibrary.wiley.com/doi/epdf/10.1002/wea.1911

Prothero, D. R., & Schwab, F. (2014) *Sedimentary Geology. An Introduction to Sedimentary Rocks and Stratigraphy* (3 ed.) New York: W.H. Freeman and Company

Rowell, C. (2011). *Geophysical Analysis of Structures and Flow Geometry of the Blue Dragon Lava Flow, Idaho,USA.* Degree project, (Department of Geoscience, Alberta). Retrieved from: https://www.researchgate.net/publication/286930465_Geophysical_analysis_of_structures_and_flow_geometry_of_the_Blue_Dragon_lava_flow_Idaho_USA/stats

Sandmeier, K.J. (2020) GPR 2D-import and processing. Retrieved 2020-05-06 from: https://www.sandmeier-geo.de/guides-and-videos.html